J. Non-Newtonian Fluid Mech. 165 (2010) 247–262

Contents lists available at ScienceDirect

Journal of Non-Newtonian Fluid Mechanics

journal homepage: www.elsevier.com/locate/jnnfm

Numerical solution of the PTT constitutive equation for unsteady three-dimensional free surface flows

M.F. Tomé[a,*], G.S. Paulo[a,1], F.T. Pinho[b], M.A. Alves[c]

[a] Departamento de Matemática Aplicada e Estatística, Instituto de Ciências Matemáticas e de Computação, Universidade de São Paulo, Av. Trabalhador Sãocarlense, 400 - Caixa Postal 668, CEP 13560-970, São Carlos, SP, Brazil
[b] CEFT - Departamento de Engenharia Mecânica - Faculdade de Engenharia da Universidade do Porto Rua Dr. Roberto Frias s/n, 4200-465 Porto, Portugal
[c] CEFT - Departamento de Engenharia Química - Faculdade de Engenharia da Universidade do Porto, Rua Dr. Roberto Frias s/n, 4200-465 Porto, Portugal

ARTICLE INFO

Article history:
Received 18 June 2009
Received in revised form 5 November 2009
Accepted 23 December 2009

Three-dimensional viscoelastic flow
Free surface
PTT model
Finite difference
Marker-and-cell
Jet buckling
Extrudate swell

ABSTRACT

This work deals with the development of a numerical technique for simulating three-dimensional viscoelastic free surface flows using the PTT (Phan-Thien–Tanner) nonlinear constitutive equation. In particular, we are interested in flows possessing moving free surfaces. The equations describing the numerical technique are solved by the finite difference method on a staggered grid. The fluid is modelled by a Marker-and-Cell type method and an accurate representation of the fluid surface is employed. The full free surface stress conditions are considered. The PTT equation is solved by a high order method, which requires the calculation of the extra-stress tensor on the mesh contours. To validate the numerical technique developed in this work flow predictions for fully developed pipe flow are compared with an analytic solution from the literature. Then, results of complex free surface flows using the PTT equation such as the transient extrudate swell problem and a jet flowing onto a rigid plate are presented. An investigation of the effects of the parameters ε and ξ on the extrudate swell and jet buckling problems is reported.

1. Introduction

Industrial flows of viscoelastic materials, such as polymer melts, often involve non-isothermal three-dimensional flow with multiple moving free surfaces. From a numerical point of view the corresponding free surface conditions are not yet satisfactorily dealt with. Some of the difficulties relate to the treatment of the advective terms in the rheological constitutive equation and how to accurately impose the free surface stress conditions. Nonetheless, many authors have developed a variety of numerical techniques for simulating viscoelastic free surface flows. For instance, Keunings and his co-workers were among the earliest contributors to viscoelastic two-dimensional free surface flows (e.g. [7,8,15]). Other classical works in the field were, for instance, the early attempts at simulating extrudate swell of an upper convected Maxwell (UCM) fluid by Tanner [28] and Ryan and Dutta [27]. Crochet and Keunings [10] presented a methodology for solving circular and planar extrudate swell using the Oldroyd-B model and compared favourably their numerical results with available experimental data. Literature on three-dimensional flows with moving free surfaces are scarce (e.g. [6,9,13,30,31]). Among the constitutive models used, the nonlinear Phan-Thien–Tanner (PTT) constitutive equation provides a better fitting to the rheology of polymer melts and concentrated solutions than other simpler models such as the UCM or Oldroyd-B. This fact, amongst others, motivated various researchers to solve contraction flows in two and three dimensions using the PTT model (see [2–4,35,36]), but its application to three-dimensional free surface flows has not yet been demonstrated.

In this work we present a numerical method capable of simulating three-dimensional free surface flows governed by the PTT constitutive equation. It is an extension to three dimensions of the two-dimensional technique presented by Paulo et al. [19,21]. The numerical technique is based on the discretization by the finite difference scheme on a staggered grid while the fluid is traced by a Marker-and-Cell approach [13]. The numerical results were validated against the analytic solution of Alves et al. [1] for fully developed pipe flow of PTT fluids. Then, results obtained from the simulation of three-dimensional problems involving moving free surfaces, such as jet buckling and the time-dependent extrudate swell, are given. Moreover, an investigation of the effects of the PTT parameters ε and ξ on the extrudate swell and jet buckling was performed.

* Corresponding author. Tel.: +55 16 3307 1942; fax: +55 16 3371 2238.
E-mail addresses: murilo@icmc.usp.br (M.F. Tomé), gilcilene@gmail.com (G.S. Paulo), fpinho@fe.up.pt (F.T. Pinho), mmalves@fe.up.pt (M.A. Alves).
[1] Currently at Departamento de Matemática, Estatística e Computação, Universidade Estadual Paulista, Brazil. Tel.: +55 16 3307 1942; fax: +55 16 3371 2238.

0377-0257/$ – see front matter © 2010 Elsevier B.V. All rights reserved.
doi:10.1016/j.jnnfm.2009.12.007

2. Governing equations

The equations governing incompressible isothermal flows are the mass conservation equation

$$\frac{\partial u_i}{\partial x_i} = 0, \tag{1}$$

and the equation of motion

$$\rho\frac{Du_i}{Dt} = -\frac{\partial p}{\partial x_i} + \frac{\partial \boldsymbol{\tau}_{ik}}{\partial x_k} + \rho g_i \tag{2}$$

where t is the time, u_i is the velocity vector, p is the pressure, ρ is the fluid density, g_i is the gravitational field and $\boldsymbol{\tau}_{ij}$ is the extra-stress tensor. The symbol $D/Dt = (\partial(\bullet)/\partial t) + (\partial(u_k\bullet)/\partial x_k)$ represents the material derivative. In this work we shall be concerned with flows of viscoelastic fluids governed by the nonlinear constitutive equation PTT (Phan-Thien–Tanner) (see [22])

$$f(\tau_{kk})\tau_{ij} + \lambda\overset{\square}{\tau}_{ij} = 2\eta D_{ij} \tag{3}$$

where

$$D_{ij} = \frac{1}{2}\left(\frac{\partial u_j}{\partial x_i} + \frac{\partial u_i}{\partial x_j}\right)$$

is the rate of deformation tensor, λ is the fluid relaxation time and η is the polymer viscosity coefficient. $f(\tau_{kk})$ is the linearized stress coefficient function, proposed in the original paper of Phan-Thien and Tanner [22] and is given by

$$f(\tau_{kk}) = 1 + \frac{\lambda\varepsilon}{\eta}\tau_{kk}. \tag{4}$$

The symbol $\overset{\square}{(\cdot)}$ represents the Gordon–Schowalter convected derivative defined as Eq. (5)

$$\overset{\square}{\tau}_{ij} = \frac{D\tau_{ij}}{Dt} - \tau_{jk}\left(\frac{\partial u_i}{\partial x_k} - \xi D_{ik}\right) - \tau_{ik}\left(\frac{\partial u_j}{\partial x_k} - \xi D_{jk}\right). \tag{5}$$

The positive parameters ε and ξ can be used to control viscoelastic properties, such as the amount of strain-hardening in extensional flow and the second normal stress difference coefficient in shear flow, respectively.

2.1. Problem formulation

To solve Eqs. (1)–(3) the EVSS transformation (Elastic-Viscous Stress-Splitting) [23] is adopted. This formulation splits the polymer extra-stress tensor τ_{ij} into the sum of a Newtonian contribution $2\eta D_{ij}$ and an elastic contribution represented by tensor S_{ij}, according to

$$\tau_{ij} = 2\eta D_{ij} + S_{ij}. \tag{6}$$

Back-substituting Eq. (6) into Eqs. (2), (3) and (5) we obtain the transformed equations which we write in non-dimensional form:

$$\frac{\partial u_i}{\partial t} + \frac{\partial(u_k u_i)}{\partial x_k} = -\frac{\partial p}{\partial x_i} + \frac{1}{Re}\frac{\partial^2 u_i}{\partial x_k \partial x_k} + \frac{\partial S_{ik}}{\partial x_k} + \frac{1}{Fr^2}g_i, \tag{7}$$

$$f(S_{kk})S_{ij} + We\overset{\square}{S}_{ij} = 2\frac{1}{Re}[1 - f(S_{kk})]D_{ij} - 2\frac{We}{Re}\overset{\square}{D}_{ij} \tag{8}$$

where $f(S_{kk}) = 1 + \varepsilon ReWe(S_{kk})$; $Re = \rho UL/\eta$, $We = \lambda U/L$ and $Fr = U/\sqrt{Lg}$ denote the Reynolds, Weissenberg and Froude numbers, respectively. In these non-dimensional numbers, g is the gravitational constant and U, L, ρ and η denote typical velocity, length, density and viscosity scales, respectively. Equations above were normalized according to

$$x_k = L\bar{x}_k, \qquad u_i = U\bar{u}_i, \qquad S_{ij} = \rho U^2\bar{S}_{ij}, \qquad g_i = g\bar{g}_i,$$
$$t = (L/U)\bar{t}, \qquad p = \rho U^2\bar{p},$$

where the overbars indicate the non-dimensional quantities. For conciseness the overbars were dropped in Eqs. (7) and (8), whereas the mass conservation Eq. (1) remains unchanged.

3. Boundary conditions

To solve Eqs. (1), (7) and (8) we need to specify appropriate boundary conditions for u_i. For the momentum equation, we employ the no-slip condition ($u_i = 0$) on stationary rigid boundaries. At fluid entrances (inflows) the normal velocity u_n is specified while the two tangential components u_{t_1} and u_{t_2} are set to zero. On outflows (fluid exits) we impose homogeneous Neumann conditions, namely $\partial u_n/\partial n = 0$, $\partial u_{t_1}/\partial n = 0$ and $\partial u_{t_2}/\partial n = 0$.

3.1. Free surface stress conditions

We shall consider unsteady free surface flows of a viscoelastic fluid moving into a passive atmosphere (which we may take to be at zero relative pressure). In the absence of surface tension effects the normal and tangential components of the stress must be continuous across any free surface, so that on such a surface (see Batchelor [5])

$$n_i\sigma_{ij}n_j = 0, \qquad t_{1i}\sigma_{ij}n_j = 0, \qquad t_{2i}\sigma_{ij}n_j = 0, \tag{9}$$

where n_i as before, denotes unit normal vector to the surface, t_{1i} and t_{2i} denote the two unit tangential vectors to the surface and σ_{ij} is the normalized total stress tensor given by

$$\sigma_{ij} = -p\delta_{ij} + \frac{2}{Re}D_{ij} + S_{ij}.$$

4. Computation of the stress on mesh boundaries

When solving the constitutive equation it is necessary to employ an appropriate effective method to approximate the derivatives of the advective terms in order to obtain accurate results and avoid unphysical solutions. In this work we employ the high order stabilized upwind scheme CUBISTA developed by Alves et al. [2] for viscoelastic models. This scheme requires the values of a generic variable, say ϕ, that can be positioned upstream (ϕ_U), downstream (ϕ_D) or remote-upstream (ϕ_R) with respect to a reference point (see Fig. 1) at which the variable is being approximated (ϕ_P). Therefore, when calculating the advective terms of the stress equations near boundaries, the values of the components of the non-Newtonian stress tensor on mesh boundaries

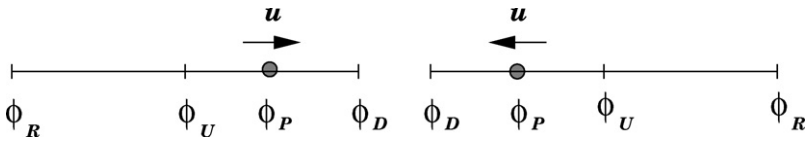

Fig. 1. Reference points used for the CUBISTA upwind scheme.

are required. We point out that many authors do not compute the non-Newtonian stress tensor on rigid boundaries and therefore when calculating the non-Newtonian stress tensor on points that lie near the boundaries (e.g. rigid walls, outflows) they employ a lower order method, often the first order upwind scheme.

To compute the non-Newtonian stress tensor on rigid walls we employ a methodology similar to that used by Tomé et al. [33] for the flow of an Oldroyd-B fluid in two dimensions. First we make the change of variables $S_{ij} = e^{-(1/We)t}\tilde{S}_{ij}$ in Eq. (8) and obtain the equation:

$$e^{-\frac{1}{We}t}[f(\tilde{S}_{ij}) - 1]\tilde{S}_{ij} + We\overset{\square}{\tilde{S}}_{ij} = 2\frac{1}{Re}[1 - f(\tilde{S}_{ij})]D_{ij} - 2e^{\frac{1}{We}t}\frac{We}{Re}\overset{\square}{D}_{ij}. \tag{10}$$

Eq. (10) provides a (6×6)-nonlinear system for the components of tensor $\tilde{S}_{ij}$. We use the no-slip condition and solve this system analytically. The details of the analytic solution of this nonlinear system are given in Appendix A.

4.1. Computation of the non-Newtonian stress tensor on inflow and outflow boundaries

These can be specified as follows:

Inflow boundary: If the velocity at the fluid entrance u_n is constant then we follow the strategy of Crochet and Marchal [16] and Mompean and Deville [17], namely:

$$S_{ij} = 0.$$

For fully developed pipe flows there is a complete analytic solution of the stress equations which is given in Section 7.

Outflow boundary: At the fluid exit, we impose homogeneous Neumann conditions for the components of non-Newtonian stress tensor (see [17,33]) namely

$$\frac{\partial S_{ij}}{\partial n} = 0.$$

5. GENSMAC-PTT3D

The method of solution is based on the ideas of Tomé et al. [31] for an Oldroyd-B fluid. It is an extension of the numerical method developed by Paulo et al. [21] for simulating two-dimensional viscoelastic free surface flows governed by the PTT model. We solve the momentum equations followed by the solution of the constitutive equation. Thus, to solve Eqs. (1), (7) and (8) we proceed as follows.

We assume that at time t_0 the velocity field $u_i(x_l, t_0)$ and the non-Newtonian stress tensor $S_{ij}(x_l, t_0)$ are known and the values of u_i and S_{ij} on the boundary are given. The new fields $u_i(x_l, t)$, $p(x_l, t)$ and $S_{ij}(x_l, t)$, at the new time level $t = t_0 + \delta t$, are calculated as follows:

Step 1: Let $\tilde{p}(x_l, t)$ be a pressure field that satisfies the correct pressure condition on the free surface (9).

Step 2: Calculate the intermediate velocity field $\tilde{u}_i(x_l, t)$ from the momentum equation

$$\frac{\partial \tilde{u}_i}{\partial t} = -\frac{\partial(u_k u_i)}{\partial x_k} - \frac{\partial \tilde{p}}{\partial x_i} + \frac{1}{Re}\frac{\partial^2 u_i}{\partial x_k \partial x_k} + \frac{\partial S_{ik}}{\partial x_k} + \frac{1}{Fr^2}g_i, \tag{11}$$

with $\tilde{u}_i(x_l, t) = u_i(x_l, t_0)$ and it must obey the same boundary conditions of velocity $u_i(x_l, t)$.

Step 3: Solve the Poisson equation for the potential function $\psi(x_l, t)$

$$\frac{\partial^2 \psi(x_l, t)}{\partial x_k \partial x_k} = \frac{\partial \tilde{u}_k(x_l, t)}{\partial x_k} \tag{12}$$

subject to the boundary conditions (see Tomé and McKee [34]): $\partial\psi/\partial n = 0$ on rigid boundary and inflows and $\psi = 0$ on free surfaces and outflows.

Step 4: Compute the final velocity

$$u_i(x_l, t) = \tilde{u}_i(x_l, t) - \frac{\partial \psi(x_l, t)}{\partial x_k}. \tag{13}$$

Step 5: Compute the pressure field from (see Tomé et al. [32])

$$p(x_l, t) = \tilde{p}(x_l, t) + \frac{\psi(x_l, t)}{\delta t}. \tag{14}$$

Step 6: Calculation of the non-Newtonian tensor $S_{ij}(x_l, t)$

6.1 Update the non-Newtonian tensor on rigid boundaries according to the equations derived in Section 4.

6.2 Update the non-Newtonian tensor on inflows and outflows according to the equations given in Section 4.1.

6.3 Compute the non-Newtonian tensor $S_{ij}(x_l, t)$ elsewhere from Eq. (8).

Step 7: Update the markers positions: the last step in the calculation is to move the markers to their new positions. This is performed by solving

$$\frac{dx_i}{dt} = u_i, \tag{15}$$

for each particle. The fluid surface is defined by a piecewise linear surface composed of triangles and quadrilaterals having marker particles on their vertices. For details see Castelo et al. [9].

6. Finite difference approximation

The equations presented in the previous section for three-dimensional Cartesian flows are solved by a finite difference method on a staggered grid. In the following we denote the velocity vector u_i by its components u, v and w along directions x, y and z, respectively. A typical cell of dimensions $\delta x \times \delta y \times \delta z$ is displayed in Fig. 2. The components of the non-Newtonian tensor S_{ij} together with the pressure field are stored at the centre of a cell, while the velocity components u, v and w are staggered by $\delta x/2$, $\delta y/2$ and $\delta z/2$, respectively.

As the fluid is continuously moving, a procedure for identifying the fluid region and the free surface is employed. To do this,

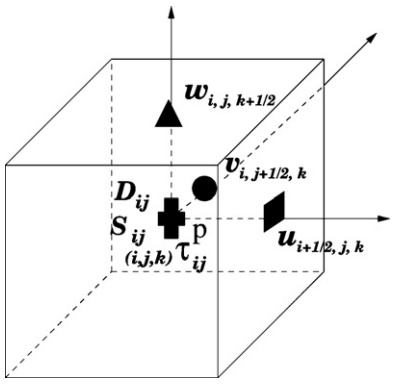

Fig. 2. Typical cell for calculation.

the cells within the mesh are flagged as: Empty (E) – cells that do not contain fluid; Full (F) – Cells full of fluid that do not share a face with an Empty cell; Surface (S) – Cells that contain fluid and share at least one face with an Empty cell (these cells contain the free surface); Boundary (B) – Cells that define a rigid boundary, where the no-slip condition is verified; Inflow (I) – Cells that define an inflow boundary; Outflow (O) – Cells that define an outflow boundary.

The time derivative in the intermediate velocity field Eq. (11) is approximated by the explicit Euler method while the linear spatial terms are approximated by central differences. The advective terms are approximated by the CUBISTA method. Details of this high order upwind scheme can be found in Alves et al. [2]. For instance, the x-component momentum Eq. (7) is approximated by the following finite difference equation

$$\begin{aligned}\tilde{u}_{i+\frac{1}{2},j,k} &= u_{i+\frac{1}{2},j,k}+\delta t\left[-\mathcal{A}(uu)_{i+\frac{1}{2},j,k}-\mathcal{A}(vu)_{i+\frac{1}{2},j,k}-\mathcal{A}(wu)_{i+\frac{1}{2},j,k}\right.\\ &-\frac{\tilde{p}_{i+1,j,k}-\tilde{p}_{i,j,k}}{\delta x}+\frac{1}{Re}\left(\frac{u_{i-\frac{1}{2},j,k}-2u_{i+\frac{1}{2},j,k}+u_{i+\frac{3}{2},j,k}}{\delta x^2}\right.\\ &+\frac{u_{i+\frac{1}{2},j-1,k}-2u_{i+\frac{1}{2},j,k}+u_{i+\frac{1}{2},j+1,k}}{\delta y^2}\\ &\left.\left.+\frac{u_{i+\frac{1}{2},j,k-1}-2u_{i+\frac{1}{2},j,k}+u_{i+\frac{1}{2},j,k+1}}{\delta z^2}\right)\right.\\ &+\frac{S^{xx}_{i+1,j,k}-S^{xx}_{i,j,k}}{\delta x}+\frac{S^{yx}_{i+\frac{1}{2},j+\frac{1}{2},k}-S^{yx}_{i+\frac{1}{2},j-\frac{1}{2},k}}{\delta y}\\ &\left.+\frac{S^{zx}_{i+\frac{1}{2},j,k+\frac{1}{2}}-S^{zx}_{i+\frac{1}{2},j,k-\frac{1}{2}}}{\delta z}+\frac{1}{Fr^2}g_x\right],\end{aligned} \tag{16}$$

where the advective terms $\mathcal{A}(uu)_{i+(1/2),j,k}$, $\mathcal{A}(vu)_{i+(1/2),j,k}$ and $\mathcal{A}(wu)_{i+(1/2),j,k}$ are approximated by the CUBISTA method and the subscripts i, j, k denote the location in the mesh where the quantities are calculated. Terms like $S^{yx}_{i+(1/2),j+(1/2),k}$ are obtained by averaging the nearest neighbours, for instance,

$$S^{yx}_{i+\frac{1}{2},j+\frac{1}{2},k}=\frac{S^{yx}_{i,j,k}+S^{yx}_{i+1,j,k}+S^{yx}_{i,j+1,k}+S^{yx}_{i+1,j+1,k}}{4}.$$

Here, and elsewhere when necessary, the components of the tensors S_{ij} and D_{ij} are indicated by superscripts, for conciseness. The difference equations for the y and z-components of the momentum equation are obtained similarly.

The Poisson Eq. (12), the final velocity correction (13) and the pressure Eq. (14) are equal to the corresponding equations for Newtonian flows. Therefore, the corresponding approximations for Eqs. (12), (13) and (14) using finite differences can be found in Tomé et al. [30] (for reasons of space they are not presented here).

The constitutive Eq. (8) is approximated by finite differences and applied at cell centres. The time derivative and the linear spatial derivatives are approximated by the explicit Euler method and by central differences, respectively. Attention is given to the advective terms which are discretized by using the high order upwind CUBISTA method [2]. For instance, the x-component of the modified constitutive Eq. (8) is approximated by the following finite difference equation

$$\begin{aligned}(S^{xx}_{i,j,k})^{(n+1)} &= S^{xx}_{i,j,k}+\delta t\left\{-\frac{1}{We}(f(S_{kk}))|_{i,j,k}S^{xx}_{i,j,k}-\mathcal{A}(uS_{xx})_{i,j,k}\right.\\ &-\mathcal{A}(vS_{xx})_{i,j,k}-\mathcal{A}(wS_{xx})_{i,j,k}+2(1-\xi)D^{xx}_{i,j,k}S^{xx}_{i,j,k}\\ &+\left[(2-\xi)\frac{u_{i,j+\frac{1}{2},k}-u_{i,j-\frac{1}{2},k}}{\delta y}-\xi\frac{v_{i+\frac{1}{2},j,k}-v_{i-\frac{1}{2},j,k}}{\delta x}\right]S^{xy}_{i,j,k}\\ &+\left[(2-\xi)\frac{u_{i,j,k+\frac{1}{2}}-u_{i,j,k-\frac{1}{2}}}{\delta z}-\xi\frac{w_{i+\frac{1}{2},j,k}-w_{i-\frac{1}{2},j,k}}{\delta x}\right]S^{xz}_{i,j,k}\\ &+\frac{2}{ReWe}[1-f(S_{kk})|_{i,j,k}]D^{xx}_{i,j,k}-\frac{2}{Re}\left(\frac{D^{xx(n+1)}_{i,j,k}-D^{xx}_{i,j,k}}{\delta t}\right.\\ &+(\mathcal{A}(uD_{xx})+\mathcal{A}(vD_{xx})+\mathcal{A}(wD_{xx}))_{i,j,k}-2(1-\xi)(D^{xx}_{i,j,k})^2\\ &-\left[(2-\xi)\frac{u_{i,j+\frac{1}{2},k}-u_{i,j-\frac{1}{2},k}}{\delta y}-\xi\frac{v_{i+\frac{1}{2},j,k}-v_{i-\frac{1}{2},j,k}}{\delta x}\right]D^{xy}_{i,j,k}\\ &\left.\left.-\left[(2-\xi)\frac{u_{i,j,k+\frac{1}{2}}-u_{i,j,k-\frac{1}{2}}}{\delta z}-\xi\frac{w_{i+\frac{1}{2},j,k}-w_{i-\frac{1}{2},j,k}}{\delta x}\right]D^{xz}_{i,j,k}\right)\right\},\end{aligned} \tag{17}$$

where,

$$\begin{aligned}D^{xx}_{i,j,k}&=\left(\frac{u_{i+(1/2),j,k}-u_{i-(1/2),j,k}}{\delta x}\right),\\ D^{xy}_{i,j,k}&=\frac{1}{2}\left(\frac{u_{i,j+(1/2),k}-u_{i,j-(1/2),k}}{\delta y}+\frac{v_{i+(1/2),j,k}-v_{i-(1/2),j,k}}{\delta x}\right),\\ D^{xz}_{i,j,k}&=\frac{1}{2}\left(\frac{u_{i,j,k+(1/2)}-u_{i,j,k-(1/2)}}{\delta z}+\frac{w_{i+(1/2),j,k}-w_{i-(1/2),j,k}}{\delta x}\right),\end{aligned} \tag{18}$$

and $f(S_{kk})|_{i,j,k}=1+\varepsilon ReWe(S^{xx}_{i,j,k}+S^{yy}_{i,j,k}+S^{zz}_{i,j,k})$.

In Eq. (17) terms which are not defined at cell positions are obtained by averaging, e.g.

$$w_{i+\frac{1}{2},j,k}:=\frac{w_{i,j,k+(1/2)}+w_{i+1,j,k+(1/2)}+w_{i,j,k-(1/2)}+w_{i+1,j,k-(1/2)}}{4}.$$

The finite difference equations for the components S_{yy}, S_{zz}, S_{xy}, S_{yz} and S_{xz} are similar to Eq. (17).

6.1. Approximation of the components of non-Newtonian stress tensor on rigid boundaries

When computing the advective terms of Eq. (17) using the CUBISTA scheme on nodes adjacent to a rigid boundary the value of S_{xx} on the boundary cells is required. The derivation of the equations for calculating the non-Newtonian stress tensor on rigid boundaries is lengthy and for this reason it is considered in Appendix A and their discretization is presented in Appendix B.

6.2. Free surface stress conditions

By taking $n_i=(n_x,n_y,n_z)$, $t_{1i}=(t_{1x},t_{1y},t_{1z})$ and $t_{2i}=(t_{2x},t_{2y},t_{2z})$, the stress conditions (9) can be written in Cartesian coordinates in the form of

$$\begin{aligned}\tilde{p} &= \frac{2}{Re}\left[\frac{\partial u}{\partial x}n_x^2+\frac{\partial v}{\partial y}n_y^2+\frac{\partial w}{\partial z}n_z^2+\left(\frac{\partial v}{\partial x}+\frac{\partial u}{\partial y}\right)n_xn_y\right.\\ &\left.+\left(\frac{\partial w}{\partial x}+\frac{\partial u}{\partial z}\right)n_xn_z+\left(\frac{\partial w}{\partial y}+\frac{\partial v}{\partial z}\right)n_yn_z\right]\\ &+S_{xx}n_x^2+S_{yy}n_y^2+S_{zz}n_z^2+2[S_{xy}n_xn_y+S_{xz}n_xn_z+S_{yz}n_yn_z],\end{aligned} \tag{19}$$

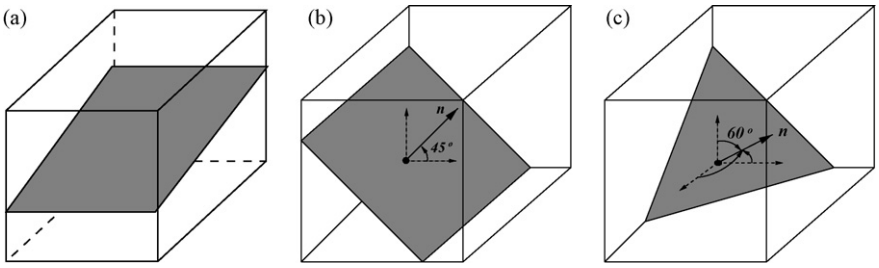

Fig. 3. Examples of plane surfaces which approximate the real free surface: (a) 1D-surface; (b) 2D-surface; (c) 3D-surface.

$$2\frac{\partial u}{\partial x}n_x t_{1x} + 2\frac{\partial v}{\partial y}n_y t_{1y} + 2\frac{\partial w}{\partial z}n_z t_{1z} + \left(\frac{\partial v}{\partial x} + \frac{\partial u}{\partial y}\right)(t_{1x}n_y + t_{1y}n_x)$$
$$+ \left(\frac{\partial w}{\partial x} + \frac{\partial u}{\partial z}\right)(t_{1x}n_z + t_{1z}n_x) + \left(\frac{\partial w}{\partial y} + \frac{\partial v}{\partial z}\right)(t_{1y}n_z + t_{1z}n_y) = \quad (20)$$
$$-Re\left[S_{xx}n_x t_{1x} + S_{yy}n_y t_{1y} + S_{zz}n_z t_{1z} + S_{xy}(t_{1x}n_y + t_{1y}n_x)\right.$$
$$\left. + S_{xz}(t_{1x}n_z + t_{1z}n_x) + S_{yz}(t_{1y}n_z + t_{1z}n_x)\right],$$

$$2\frac{\partial u}{\partial x}n_x t_{2x} + 2\frac{\partial v}{\partial y}n_y t_{2y} + 2\frac{\partial w}{\partial z}n_z t_{2z} + \left(\frac{\partial v}{\partial x} + \frac{\partial u}{\partial y}\right)(t_{2x}n_y + t_{2y}n_x)$$
$$+ \left(\frac{\partial w}{\partial x} + \frac{\partial u}{\partial z}\right)(t_{2x}n_z + t_{2z}n_x) + \left(\frac{\partial w}{\partial y} + \frac{\partial v}{\partial z}\right)(t_{2y}n_z + t_{2z}n_y) =$$
$$-Re\left[S_{xx}n_x t_{2x} + S_{yy}n_y t_{2y} + S_{zz}n_z t_{2z} + S_{xy}(t_{2x}n_y + t_{2y}n_x)\right.$$
$$\left. + S_{xz}(t_{2x}n_z + t_{2z}n_x) + S_{yz}(t_{2y}n_z + t_{2z}n_x)\right]. \quad (21)$$

To apply these conditions we follow the ideas of Tomé et al. [30]. We assume that the mesh spacing is small so that the free surface can be approximated by a set of linear surfaces. Three types of linear surfaces are considered: 1D-surface, 2D-surface and 3D-surface (see Fig. 3). The finite difference equations arising from these approximations are the same as those for an Oldroyd-B fluid and for this reason they are not presented here. Details of these finite differences can be found in Tomé et al. [31].

6.3. Time-step calculation

To increase the efficiency of the method an automatic procedure is employed to compute the time-step at each calculational cycle. We select a δt that satisfies the conditions below (written in non-dimensional form):

$$\delta t_{\mathbf{CFL}} < \frac{h}{u_i}, \quad \text{interpreted component-wise} \quad (22)$$

$$\delta t_{\mathbf{VISC}} < \begin{cases} Re\dfrac{h^2}{6}, & \text{if } Re < 1, \\ \dfrac{h^2}{6}, & \text{otherwise.} \end{cases} \quad (23)$$

where h is the mesh spacing. Inequality (22) represents the Courant–Friedrichs–Lewy (CFL) restriction while (23) gives the usual viscous restriction. The time-step selected is given by

$$\delta t = A * \min\{A_1 * \delta t_{\mathrm{CFL}}, A_2 * \delta t_{\mathrm{visc}}\},$$

where $0 < A, A_1, A_2 < 1$. The implementation of these inequalities follows the procedure described in Tomé et al. [30].

7. Validation of the approach: *fully developed pipe flow*

The analytic solution for fully developed pipe flows of PTT fluids was presented by Alves et al. [1] (see also [18] for the special case $\xi = 0$ – SPTT Model). In non-dimensional form this solution is given by Eqs. (24)–(27) below using a cylindrical Coordinate system:

$$w(r) = \frac{1}{2}\frac{Re}{\chi}\Delta p_z(1 - r^2) + \frac{1}{ReWe^2\xi(2-\xi)\Delta p_z}\left(1 + \frac{2}{\chi}\right)\left[\ln\frac{1 + \sqrt{1-(ar)^2}}{1 + \sqrt{1-a^2}}\right.$$
$$\left. + \left(1 + \sqrt{1-a^2}\right) - \left(1 + \sqrt{1-(ar)^2}\right)\right], \quad (24)$$

$$\tau_{zr}(r) = \frac{1}{2}\Delta p_z r, \quad (25)$$

$$\tau_{zz}(r) = \frac{1}{2ReWe\xi}\left(1 - \sqrt{1.0 - (ar)^2}\right), \; ar \le 1, \quad (26)$$

$$\tau_{rr}(r) = -\frac{\xi}{(2-\xi)}\tau_{zz}(r), \quad (27)$$

where $a = -ReWe\Delta p_z\sqrt{\xi(2-\xi)}$, $\xi \le 2$ and $\chi = \xi(2-\xi)/\varepsilon(1-\xi)$. To simulate pipe flow using the 3D numerical technique described in this paper, we need to write these equations in a Cartesian coordinate system (x, y, z) to employ them as inflow boundary condition in appropriate problems. By using a rotation matrix, it can be shown that the components of the extra-stress tensor, written in three-dimensional Cartesian coordinates, are given by

$$\tau_{xx}(x,y) = -\frac{x^2}{2ReWe(2-\xi)(x^2+y^2)}\left(1 - \sqrt{1 - a^2(x^2+y^2)}\right), \quad (28)$$

$$\tau_{yy}(x,y) = -\frac{y^2}{2ReWe(2-\xi)(x^2+y^2)}\left(1 - \sqrt{1 - a^2(x^2+y^2)}\right), \quad (29)$$

$$\tau_{zz}(x,y) = -\frac{1}{2ReWe\xi}\left(1 - \sqrt{1 - a^2(x^2+y^2)}\right), \quad (30)$$

$$\tau_{xy}(x,y) = -\frac{xy}{2ReWe(2-\xi)(x^2+y^2)}\left(1 - \sqrt{1 - a^2(x^2+y^2)}\right), \quad (31)$$

$$\tau_{xz}(x,y) = \frac{1}{2}\Delta p_z x, \quad (32)$$

$$\tau_{yz}(x,y) = \frac{1}{2}\Delta p_z y. \quad (33)$$

The velocity $w(x, y)$ is given by (24) where $r = \sqrt{x^2+y^2}$ and $u = v = 0$.

We validated the treatment of the viscoelastic extra-stress tensor on rigid boundaries and on interior points by simulating pipe filling followed by pipe flow. We considered a pipe of radius R and length $5R$. At the pipe entrance we imposed the analytic values

of the velocity $w(x, y)$ given by (24) as well the analytic values of the components of the non-Newtonian tensor, $S_{xx}(x, y)$, $S_{yy}(x, y)$, $S_{zz}(x, y)$, $S_{xy}(x, y)$, $S_{xz}(x, y)$ and $S_{yz}(x, y)$ according to Eqs. (28)–(33) (we recall that S_{ij} and τ_{ij} are related by the EVSS formulation (see Eq. (6))). At the pipe walls the velocity satisfied the no-slip condition (in this paper the walls do not move) and the non-Newtonian tensor S_{ij} was calculated by the equations derived in Section 4. At the pipe exit the velocity satisfied the conditions given on Section 3 and the non-Newtonian tensor S_{ij} satisfied the homogeneous Neumann condition (see Section 4.1).

The simulation started with the pipe empty and the fluid was injected through the pipe entrance which was gradually filled. Initially, there was a free surface within the pipe. On the free surface of the fluid the boundary conditions were the free surface stress conditions presented in Section 3.1. The numerical solutions were calculated using the numerical method presented in Section 5.

We simulated the pipe flow with the following input data and scaling parameters: $\varepsilon = 0.2$, $\xi = 0.15$, $R = L = 1.0\,\text{cm}$, $U = 1.0\,\text{cm s}^{-1}$, $\rho = 1000\,\text{kg m}^{-3}$, $\eta = 0.13333\,\text{Pa s}$ and $\lambda = 0.6\,\text{s}$, so that $Re = 0.75$ and $We = 0.6$. The normalized value $\Delta p_z = -3.9054$ was chosen so that $w_{\max} = w(0, 0) = 1$ (see Eq. (24)), i.e., the velocity scale used in the non-dimensionalization (U) was the centreline velocity.

To analyse the convergence of GENSMAC3D-PTT on this problem we computed the numerical solution on three meshes:

M12: $12 \times 12 \times 60$ cells (12 cells across the diameter),
M16: $16 \times 16 \times 80$ cells (16 cells across the diameter),
M20: $20 \times 20 \times 100$ cells (20 cells across the diameter).

We simulated the pipe flow until steady state was achieved and calculated the numerical solutions at the cross-section $z = 5R/2$ for meshes M12, M16 and M20. We performed 3D-plotting with both numerical and analytic solutions and the 3D plots displayed good agreement between the two solutions. However, for ease of understanding we present two-dimensional plots of the results only. Thus, we shall either fix $y = 0.5$ and vary x or fix $x = 0.5$ and vary y, i.e., the profiles shown are off centred. Note that by choosing $x = 0$ the analytic expressions for τ_{xx}, τ_{xy} and τ_{xz} show that they vanish (τ_{yy}, τ_{xy} and τ_{yz} also vanish if we choose $y = 0$). The numerical solutions together with the analytic solutions are displayed in Figs. 4 and 5.

We can observe in Figs. 4 and 5 that the numerical solutions obtained using the three meshes are in good agreement with the analytic solutions. Moreover, we can see that as the mesh is refined the numerical solutions converge to the analytic solutions.

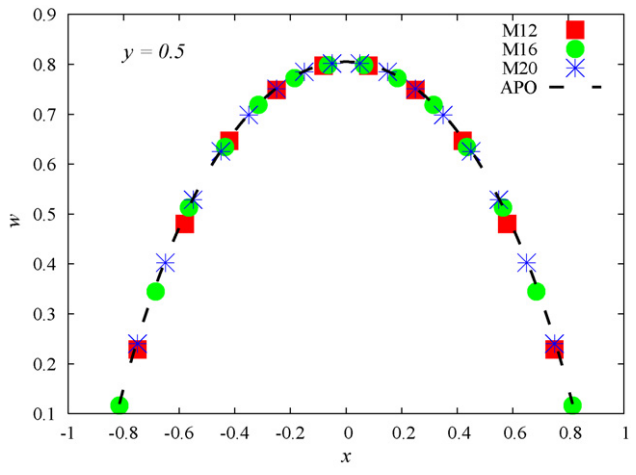

Fig. 4. Numerical and analytic solutions of the velocity w at time $t = 50\,\text{s}$. Results shown at $y = 0.5$ and $z = 5/2$. APO refers to Alves et al. [1] analytic solution.

To confirm the convergence of GENSMAC3D-PTT for each simulation we computed the relative errors between the exact solution ($\boldsymbol{\tau}_{ij}$) and the numerical solutions ($\boldsymbol{\tau}^*_{ij}$) as

$$E(\boldsymbol{\tau}) = \sqrt{\frac{\sum_{(i,j)} (\boldsymbol{\tau}_{ij} - \boldsymbol{\tau}^*_{ij})^2}{\sum_{(i,j)} \boldsymbol{\tau}^2_{ij}}}. \tag{34}$$

Table 1 shows the errors obtained on the three meshes while Fig. 6 displays the errors as a function of the mesh spacing h. Table 1 shows that the errors decrease with mesh refinement with those for velocity being very small ($E(w) \ll 1\%$) and those of stress being larger but not exceeding 4% in the finer mesh. These results validate the numerical method developed in this work for solving the PTT model for three-dimensional flows.

8. The effects of ε and ξ on extensional and shear viscosities

The dimensionless shear and extensional viscosities are shown in Fig. 7 for a range of ε and ξ values. In Fig. 7(a) we illustrate the influence of the ε parameter, keeping $\xi = 0.03$, and in Fig. 7(b) the influence of ξ for $\varepsilon = 0.01$. It is clear that ε influences mostly the extensional viscosity, and for small values of ε the plateau of the extensional viscosity at high strain rates is found to be inversely proportional to this parameter. On the other hand, parameter ξ influences mostly the shear viscosity with shear thinning taking place at lower shear rates as ξ increases.

For high ε values (about 0.5) the extensional viscosity does not increase significantly above the Newtonian plateau, and a quasi-Newtonian behaviour is expected under strong extensional flow. In fact, for $\varepsilon > 0.5$ an inversion in the extensional viscosity behaviour is observed, with a minimum value occurring at high strain rates, in deep contrast with the behaviour at lower ε values, where higher extensional viscosities are found.

In summary, Fig. 7 shows that the effects of viscoelasticity provided by the PTT model will be stronger if ε and ξ are small.

9. Numerical simulation of the time-dependent extrudate swell

When a jet of fluid leaves a tube and flows into the air then under certain circumstances the diameter of the jet can become significantly larger than the diameter of the tube. This phenomenon is known as extrudate swell and it is an important effect caused by viscoelasticity. It occurs mainly because of the effects associated to the first normal stress difference at the tube exit. Many applications in the polymer industry suffer from this problem and many researchers have developed a fair amount of numerical techniques to simulate the extrudate swell both in two- and three-dimensions (e.g. [10,14,15,27,28,31,33], to mention only a few). The swelling ratio is defined by $S_r = (D_{\max} - D)/D$, where $D_{\max}$ represents the maximum diameter of the extrudate and D is the tube diameter.

We shall demonstrate that GENSMAC3D-PTT can simulate the transient extrudate swell of highly viscoelastic jets. The three-dimensional viscoelastic jet emerging from a pipe was simulated imposing at the pipe exit the velocity and stress fields corresponding to fully developed flow. For the Reynolds numbers under consideration, it would be more realistic to impose fully developed flow conditions at a plane upstream of the exit and to let the flow evolve and adapt prior to exit. However, since our purpose was essentially that of assessing the code performance in free flow, the fully developed conditions were imposed right at the exit. Therefore, the simulations started with the fluid emerging into the atmosphere through the pipe exit. When the jet emerges into the

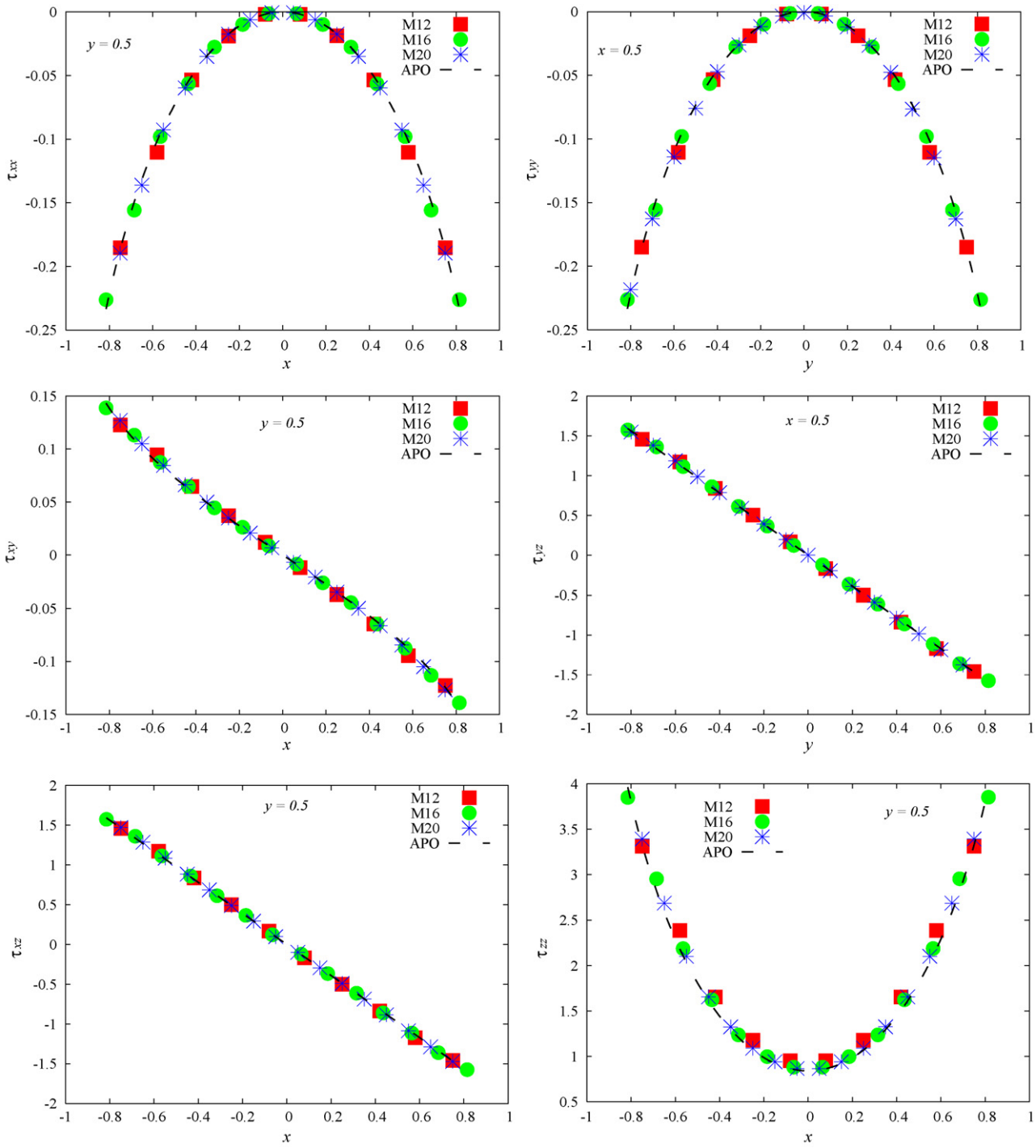

Fig. 5. Numerical and analytic solutions at time $t = 50$ s. Components τ_{xx}, τ_{zz}, τ_{xy}, τ_{xz} are shown at $y = 0.5$ and $z = 5/2$ while components τ_{yy} and τ_{yz} were evaluated at $x = 0.5$ and $z = 5/2$. APO refers to Alves et al. [1] analytic solution.

Table 1
Errors of the numerical solutions obtained on various meshes according to Eq. (34).

Mesh	$E(w)$	$E(\tau_{xx})$	$E(\tau_{yy})$	$E(\tau_{zz})$	$E(\tau_{xy})$	$E(\tau_{xz})$	$E(\tau_{yz})$
$M12$	0.00982	0.0671	0.0671	0.0640	0.0599	0.0268	0.0268
$M16$	0.00707	0.0370	0.0371	0.0390	0.0474	0.0139	0.0140
$M20$	0.00258	0.0331	0.0331	0.0329	0.0327	0.0104	0.0104

Reference is the analytic solution of Alves et al. [1].

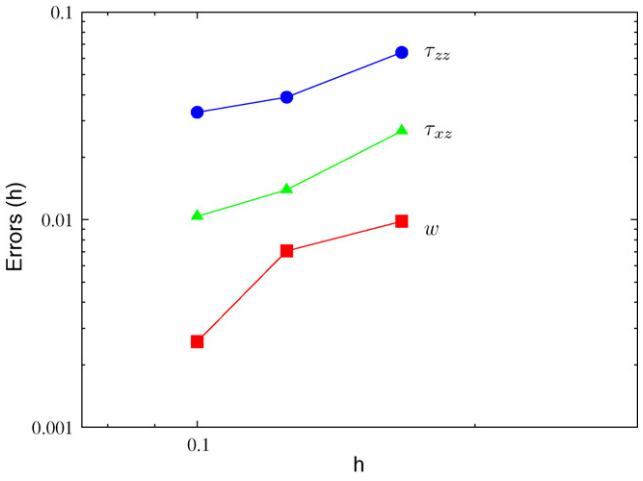

Fig. 6. Decrease of the errors as a function of the mesh spacing h.

air, it continues to flow moving the free surface in the atmosphere. On the free surface of the fluid the boundary conditions were those presented in Section 3.1. A circular outflow boundary with diameter of $6R$ was colocated at a distance of $10R$ from the pipe exit. Fig. 8 displays the domain and the objects used in the simulations of the transient extrudate swell. We performed several simulations where we fixed the Reynolds number and varied the Weissenberg number.

The input data used were $\varepsilon = 0.3$, $\xi = 0.01$, $L = R = 1\,\text{cm}$ (radius of the pipe), $U = w_{\max} = 1\,\text{cm}\,\text{s}^{-1}$, $\rho = 1000\,\text{kg}\,\text{m}^{-3}$, $\eta = 0.13333\,\text{Pa}\,\text{s}$, so that $Re = 0.75$. We chose $\lambda = 0.1\,\text{s}$, $0.5\,\text{s}$, $1.0\,\text{s}$ to obtain $We = 0.1, 0.5, 1.0$, respectively. According to the analytic solution of Eq. (24), to maintain $w_{\max} = 1\,\text{cm}\,\text{s}^{-1}$ the normalized pressure gradient was set to $\Delta p_z = -5.2701, -4.3983, -3.4601$, for $We = 0.1, 0.5, 1.0$, respectively. In these simulations a dimensionless mesh spacing of $\delta x = \delta y = \delta z = 0.125$ was employed giving $(48 \times 48 \times 160)$ cells within the flow domain. Hereafter, we shall refer to this mesh as $\mathbf{M_{SWELL}}$.

Fig. 9 shows the results obtained from the simulations for $We = 0.1, 0.5, 1.0$ at times $t = 5\,\text{s}$, $17.5\,\text{s}$ and $42.5\,\text{s}$. At time $t = 5\,\text{s}$ we can already observe that larger Weissenberg numbers have

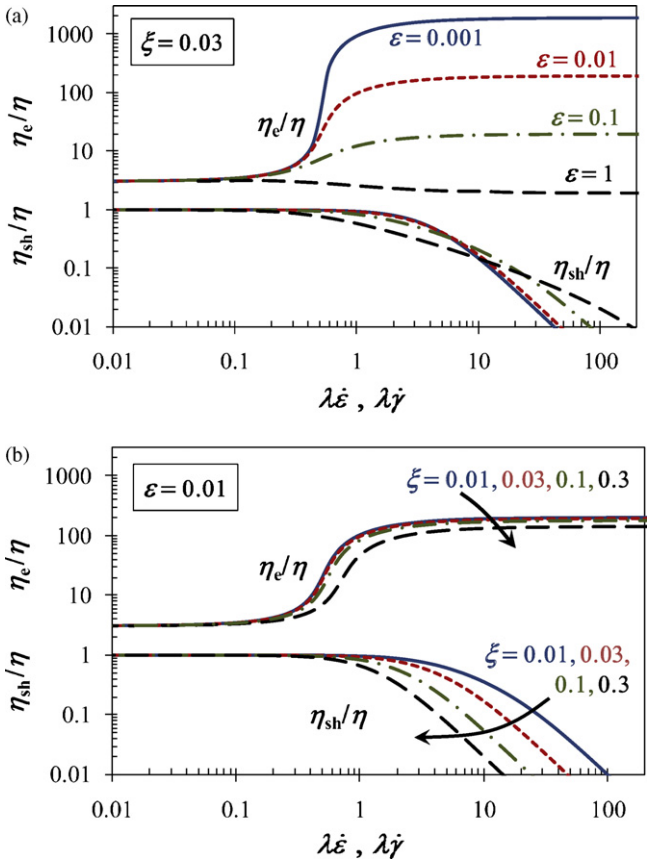

Fig. 7. Extensional viscosity (η_e) as function of the strain rate and shear viscosity as function of the shear rate for the PTT model: influence of the parameter ε for $\xi = 0.03$ (above); influence of the ξ parameter for $\varepsilon = 0.01$ (below).

larger swelling and the differences become more noticeable as time increases. At time $t = 42.5\,\text{s}$ the swelling ratios (S_r) calculated for these three flows were 11.54% for $We = 0.1$, 29.23% for $We = 0.5$ and 32.30% for $We = 1.0$. We point out that these swelling ratios do not change if the calculations are left to proceed further, hence

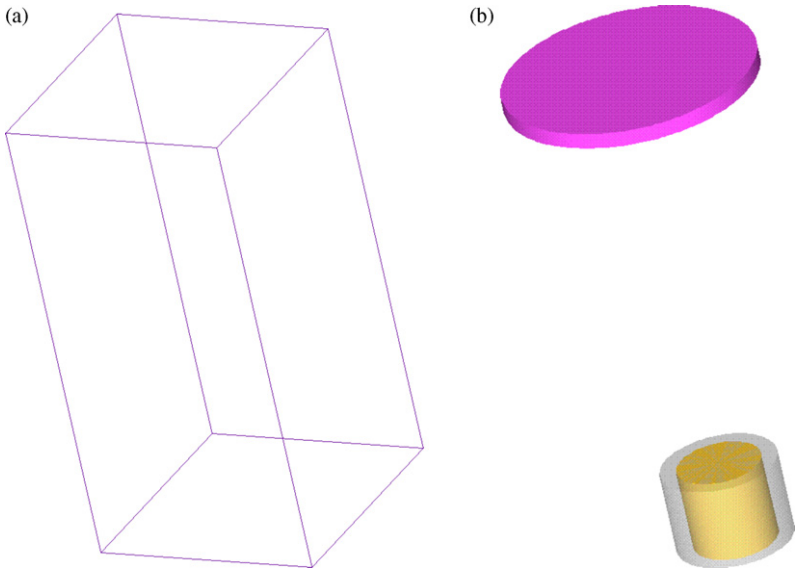

Fig. 8. Numerical simulation of the time-dependent extrudate swell: description of the flow domain. (a) Three-dimensional region; (b) Objects used: 3D-tube (gray surface), pipe exit (yellow surface) and outflow boundary (pink surface). For interpretation of the references to color in this figure legend, the reader is referred to the web version of the article.

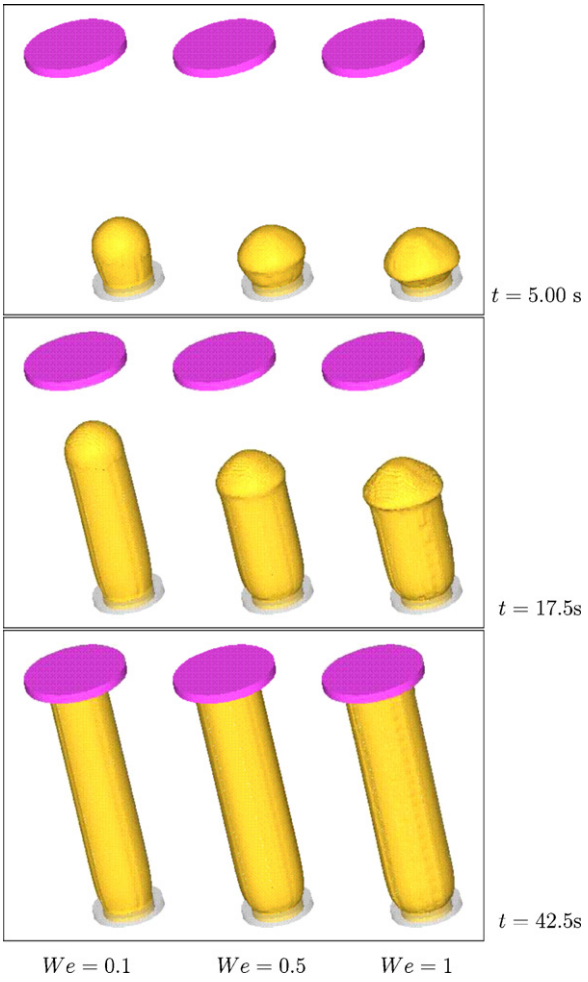

Fig. 9. Numerical solution of the time-dependent extrudate swell. Fluid flow visualization at selected times. $\varepsilon = 0.3$, $\xi = 0.01$, $Re = 0.75$ and $We = 0.1, 0.5, 1.0$.

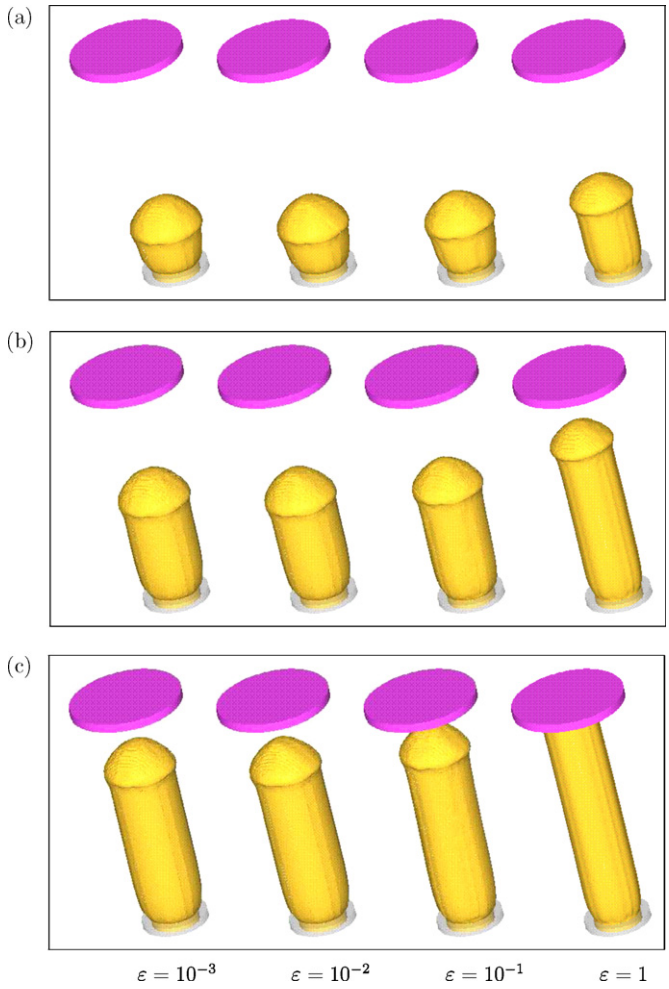

Fig. 10. Numerical simulation of the extrudate swell for various values of ε and $Re = 0.5$, $We = 0.5$, $\xi = 0.01$. Fluid flow visualization at times $t = 10$ s (a), $t = 20$ s (b) and $t = 30$ s (c).

the simulations were stopped at $t = 42.5$ s (results for $t > 42.5$ s are not shown here). The swelling ratios obtained for $We = 0.5$ and $We = 1.0$ are very similar, most probably because the value of ε used in these simulations is large. Indeed, in the next section we show that the value of parameter ε has a strong influence on the extrudate swell phenomenon, as it is anticipated from the material functions shown in Fig. 7.

9.1. The effect of the ε parameter on the extrudate swell

In this section we demonstrate that extrudate swell predicted by the PTT model is strongly affected by parameter ε. In particular, we show that for high values of ε ($\varepsilon > 0.5$), the PTT model applied to the extrudate swell can produce results similar to the Newtonian case, in accordance with the extensional viscosity behaviour illustrated in Fig. 7.

We carried out various simulations where the following data were kept fixed: $\xi = 0.01$, $L = R = 1$ cm, $U = w_{max} = 1$ cm s^{-1}, $\rho = 1000$ kg m^{-3}, $\eta = 0.2$ Pa s and $\lambda = 0.5$ s. The flow domain and the mesh employed were the same used in the previous section (see Fig. 8 and $\mathbf{M_{SWELL}}$). With these data we have $Re = 0.5$ and $We = 0.5$. To show that the ε parameter has a strong influence on the extrudate swell we performed four simulations where ε assumed the values $10^{-3}, 10^{-2}, 10^{-1}$ and 1 (cf. Fig. 7(a) for details of shear and extensional viscosity behaviour). Fig. 10 displays the three-dimensional view of the results obtained at times $t = 10$ s, 20 s and $t = 30$ s, while Fig. 11 shows a front view of the results at times $t =$ 20 s and $t = 30$ s. The variation of swelling ratio with ε is displayed in Fig. 12. Swelling decreases as ε increases and the maximum swelling ($S_r = 38.33\%$) is seen for $\varepsilon = 10^{-3}$. For $\varepsilon = 1$, and although the Weissenberg number is large ($We = 0.5$), the swelling ratio was small (21.67%), which is similar to the swell produced by GNF fluids. This variation can be understood on the basis of the extensional viscosity behaviour of the PTT fluid. Fig. 7 illustrates that as ε increases, the extensional viscosity of the fluid decreases significantly. The normal stresses in shear flow (not represented in Fig. 7) also decrease as ε increases. Thus, the effective Weissenberg number is smaller for higher values of ε, and therefore the flow becomes less elastic. The effective Weissenberg number (We^*) is determined as $We^* = \lambda(\dot\gamma)\dot\gamma$, where the characteristic shear rate is estimated as $\dot\gamma = U/L$ and the effective relaxation time as $\lambda(\dot\gamma) = \Psi_1(\dot\gamma)/[2\eta(\dot\gamma)]$, where Ψ_1 represents the first normal stress difference coefficient. The effective Weissenberg numbers for the cases shown in Fig. 11 are $We^* = 0.5, 0.498, 0.478$, and 0.386 for $\varepsilon = 10^{-3}, 10^{-2}, 10^{-1}$ and 1, respectively, thus justifying the observed behaviour in the extrudate swell for different ε values at $We = 0.5$.

9.2. The effect of parameter ξ on the extrudate swell

To show that the parameter ξ has an effect on the extrudate swell phenomenon we performed several simulations for increasing values of ξ, keeping all other data constant.

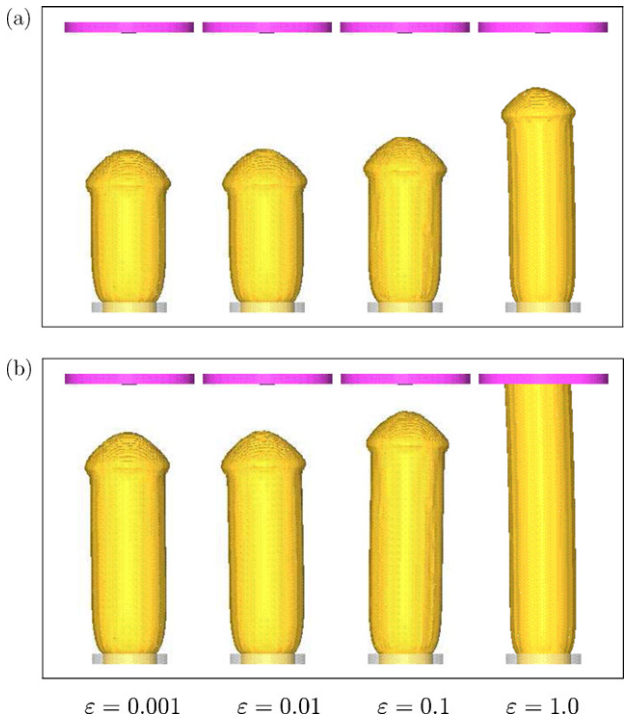

Fig. 11. Fluid flow visualization of the simulation of the extrudate swell. $Re = 0.5$, $We = 0.5$, $\xi = 0.01$. Frontal view at times $t = 20$ s (a) and $t = 30$ s (b).

The following input data were kept fixed: $L = 1$ cm (radius), $U = w_{\max} = 1\,\mathrm{cm\,s^{-1}}$, $\rho = 1000\,\mathrm{kg\,m^{-3}}$, $\eta = 0.2$ Pa s, $\varepsilon = 0.01$ and $\lambda = 0.5$ s, leading to $Re = 0.5$ and $We = 0.5$. The flow domain and the mesh employed were the same used in the previous Section (see Fig. 8 and $\mathbf{M_{SWELL}}$). We performed four simulations where the parameter ξ assumed the values of 0.001, 0.01, 0.1, 0.2, respectively. To maintain $w_{max} = 1$ in Eq. (24), for each value of ξ the normalized pressure gradient was set to $\Delta p_z = -7.368012$, -7.3177, -6.8385, -6.34025, respectively.

Fig. 13 displays the fluid flow visualization obtained from these simulations at different times while Fig. 14 shows the front view of the results at time $t = 30$ s. We can observe in both of these figures that as ξ increases from 0.01 to 0.2 the swelling decreases by a small amount of order 5%. This is confirmed in Fig. 15 where it is shown

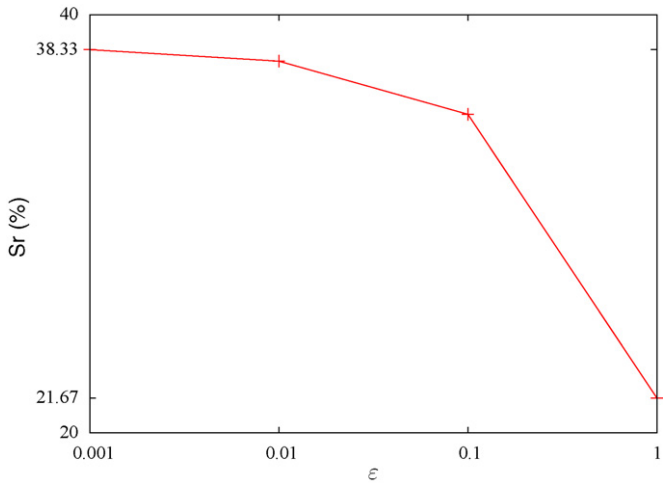

Fig. 12. Swelling ratio as a function of ε. $Re = 0.5$, $We = 0.5$, $\xi = 0.01$.

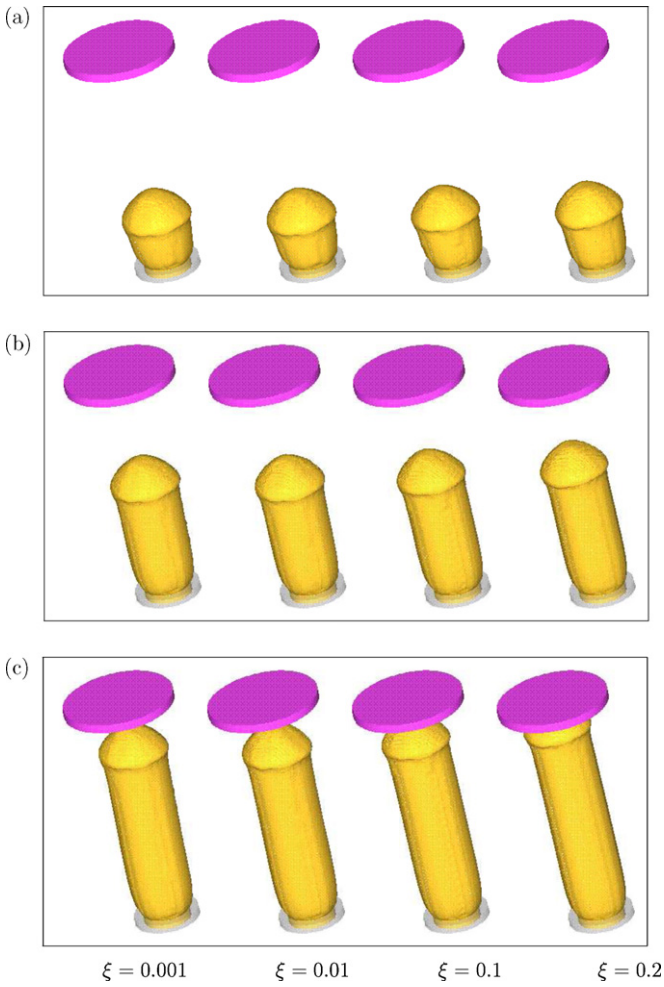

Fig. 13. Numerical simulation of the extrudate swell for various values of ξ and $Re = 0.5$, $We = 0.5$, $\varepsilon = 0.1$. Fluid flow visualization at times (a) $t = 10$ s, (b) $t = 20$ s, (c) $t = 30$ s.

that the swelling ratios vary from 30.87% at $\xi = 0.2$ to a maximum of 35.57% for $\xi = 0.001$. The effect of ξ on the extrudate swell was not too pronounced as in the case of the parameter ε. Indeed, the main effect of this parameter is on Ψ_2, and does not have a strong effect on η_E which is the more important property for this type of flow.

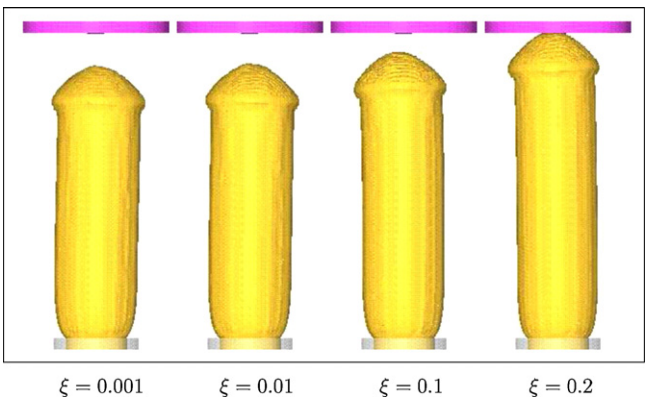

Fig. 14. Numerical solution of the time-dependent extrudate swell for various values of ξ. $Re = 0.5$, $We = 0.5$, $\varepsilon = 0.1$. Front view at time $t = 30$ s.

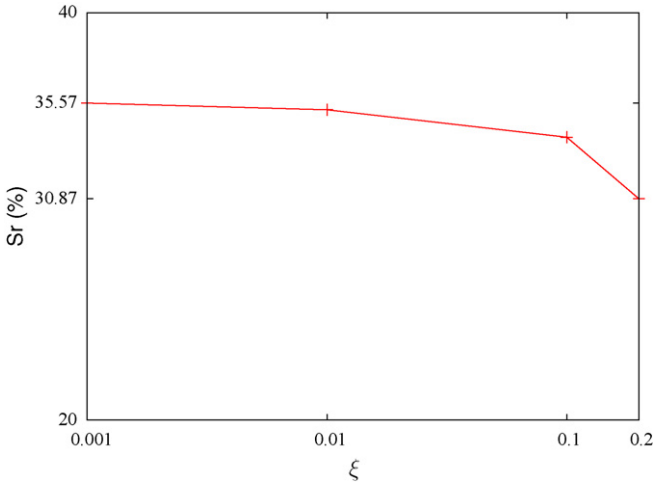

Fig. 15. Numerical solution of the time-dependent extrudate swell. $Re = 0.5$, $We = 0.5$, $\varepsilon = 0.1$. Swelling ratio as a function of ξ.

10. Numerical simulation of jet buckling

Jet buckling occurs when a jet impacts a rigid plate at small Reynolds numbers and the ratio H/D between the height of the jet and its diameter exceeds a critical value. Jet buckling has been investigated by several authors both numerically and experimentally ([6,11,12,20,21,24–26,29,31,33]), but a consistent theory explaining this instability has yet to be developed. With regard to axisymmetric Newtonian jets, Cruickshank and Munson [12] presented criteria for this instability based on experimental data. They reported jet buckling for $Re < 1.2$ and $H/D > 7.2$.

In this work we demonstrate numerically the role of viscoelasticity on the jet buckling phenomenon by performing a variety of simulations for Newtonian and PTT jets impacting a flat plate at a Reynolds number of $Re = 0.5$ and $H/D = 20$. According to Cruickshank and Munson [12] under these conditions a Newtonian jet will buckle while for the PTT jet no analysis is available yet. In these simulations, the following geometric input data were used: jet diameter $D = 6$ mm, height from the outlet to the rigid plate $H = 12$ cm, mesh spacing $\delta x = \delta y = \delta z = 1$ mm, constant inlet velocity $U = 1.0\,\mathrm{m\,s^{-1}}$, gravity acting in the Z-direction with $g_z = -9.81\,\mathrm{m\,s^{-2}}$, $\eta = 12$ Pa s, $\rho = 1000\,\mathrm{kg\,m^{-3}}$; thus $Re = UD/\nu = 0.5$. The PTT variables were: $\varepsilon = 0.01$, $\xi = 0.01$ and $\lambda = 0.006$ s, so that $We = \lambda U/D = 1.0$.

The results obtained are displayed in Fig. 16 where it can be observed that soon after jet impingement (cf. $t = 0.175$, 0.3 s), the Newtonian jet develops a cone shape geometry while the PTT jet starts buckling. Only at $t = 0.375$ s the Newtonian jet, due to viscous forces, loses its conical shape and the jet begins to become

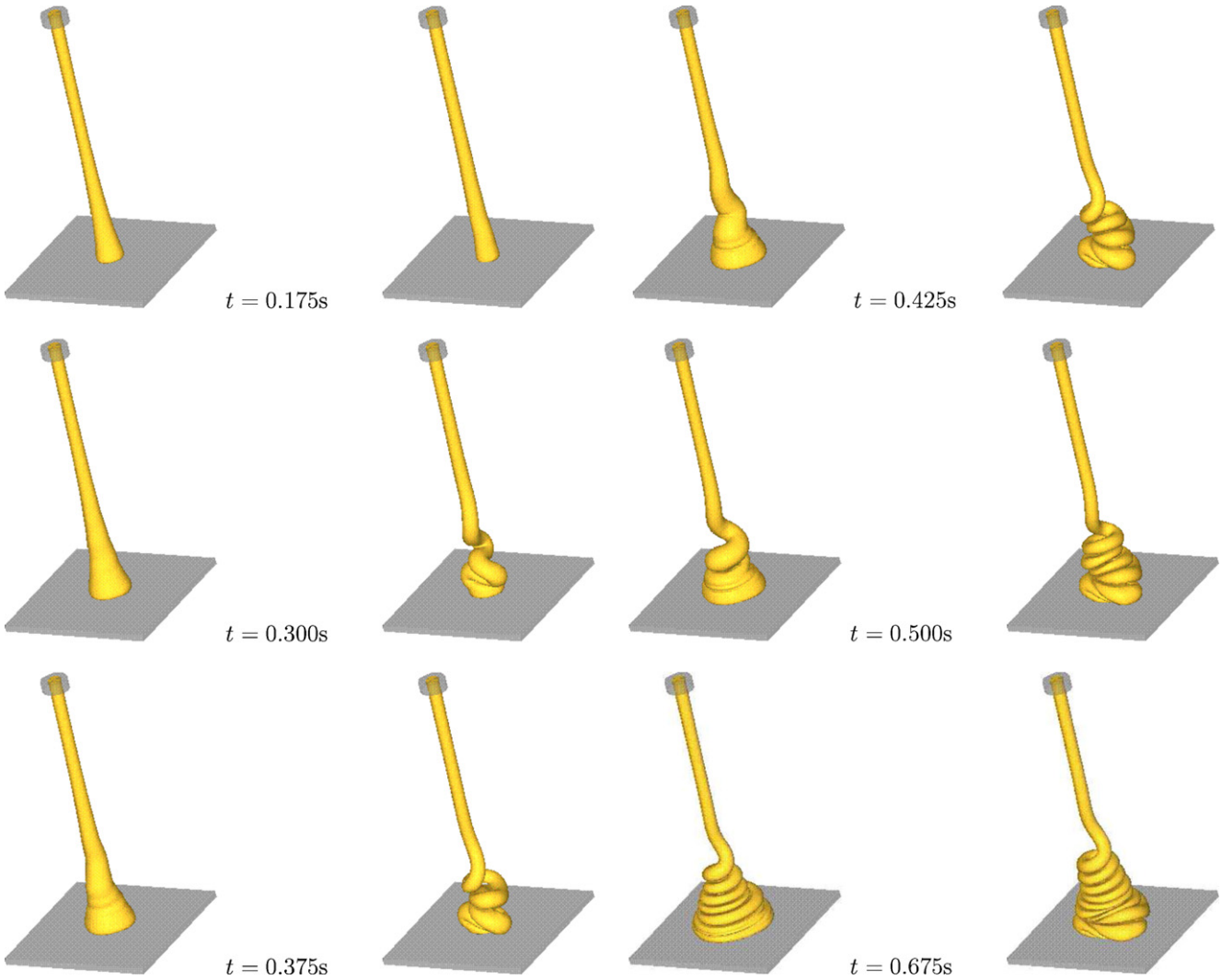

Fig. 16. Numerical simulation of jet buckling at $Re = 0.5$. Fluid flow visualization at selected times. Column 1 and 3: Newtonian fluid. Column 2 and 4: PTT fluid with $We = 1$ ($\varepsilon = \xi = 0.01$).

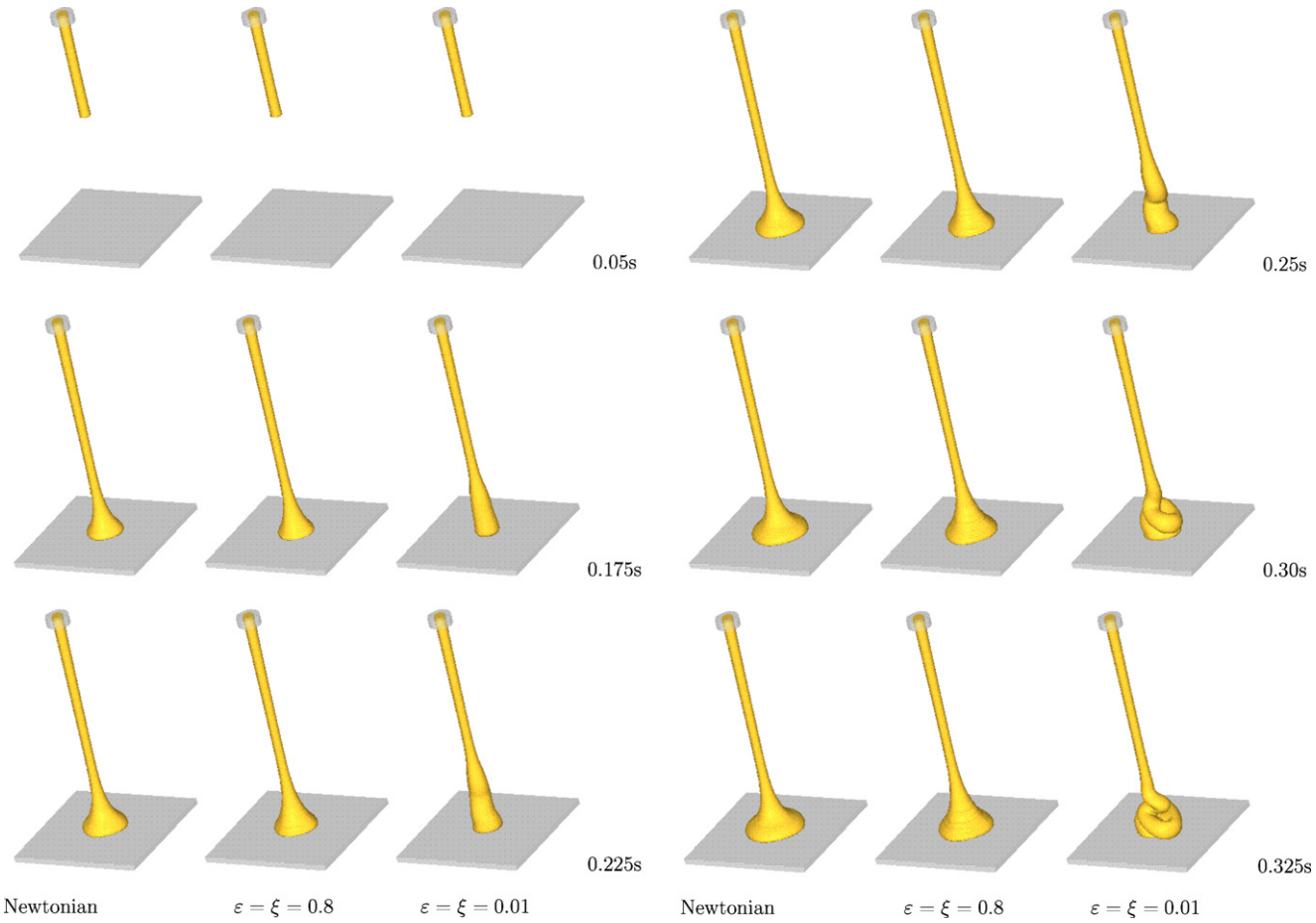

Fig. 17. Numerical simulation of a jet flowing onto a rigid surface. Fluid flow visualization at selected times. First column: Newtonian jet with $Re = 1.5$; Second column: PTT jet with $Re = 1.5$, $We = 10$ and $\varepsilon = \xi = 0.8$; Third column: PTT jet with $Re = 1.5$, $We = 10$ and $\varepsilon = \xi = 0.01$.

unstable. At subsequent times it is clear that the Newtonian jet also undergoes buckling and we can see that at time $t = 0.675$ s both jets present the coiling effect.

10.1. The effect of the ε and ξ parameters on jet buckling

The results obtained in Sections 9 and 9.1 for the extrudate swell showed that although the value of *We* was large, depending on the values selected for ε and ξ, the viscoelastic effects may not be too pronounced. A similar situation is observed in the jet buckling flow and to further demonstrate this fact we have performed three additional simulations of a jet flowing onto a rigid surface. The first simulation, illustrated in Fig. 17 shows a Newtonian jet impinging on a rigid surface with a Reynolds number of $Re = 1.5$ and $H/D = 20$ ($U = 1$ m s^{-1}, $D = 0.006$ m, $H = 12$ cm). The input data used in this Newtonian simulation were the same as those employed in Section 10, except for the lower viscosity of $\eta = 4$ Pa s required to produce $Re = 1.5$. The second simulation considered the same data used in the first simulation for the PTT model but now with parameters $\lambda = 0.06$ s, $\varepsilon = \xi = 0.8$. To show that the parameters ε and ξ can affect this problem, a third simulation using $\varepsilon = \xi = 0.01$ was performed (the other input data were kept unchanged). Therefore, in these two PTT simulations we had $Re = 1.5$ and $We = 10$, but these two non-dimensional numbers were based on zero shear rate fluid properties. As shown in Fig. 17, the differences between the results of these two PTT fluid simulations are dramatic. Indeed, according to Cruickshank's predictions the Newtonian jet did not present the buckling phenomenon and this is confirmed in our predictions where the jet flows smoothly in the radial direction. However, although the zero shear rate Weissenberg number is quite high ($We = 10$), the results from the simulation using $\varepsilon = \xi = 0.8$ display a flow behaviour similar to the Newtonian case while the simulation with $\varepsilon = \xi = 0.01$ shows that the jet has buckled. Presumably, this happened because of the increase of the extensional viscosity after the jet impinged on the solid surface which made the jet more viscous inhibiting the flow in the radial direction. This fact has been confirmed for two-dimensional PTT jets (see Paulo et al. [21]). These results demonstrate that if the values of parameters ε and ξ are large then the effect of viscoelasticity is diminished, as illustrated in the rheology plots of Fig. 7.

11. Conclusions

This paper presented a finite difference technique for solving three-dimensional free surface flows described by the Phan-Thien–Tanner constitutive equation. The numerical method described herein used a Marker-and-Cell approach to model the fluid and an accurate approximation of the free surface stress conditions was employed. The numerical method developed in this work was included into the Freeflow3D simulation system [9] extending Freeflow3D to viscoelastic flows described by PTT fluids. The flow in a three-dimensional pipe was simulated and the numerical results were compared with the corresponding analytic solutions. The agreement between the two solutions was good and mesh refinement demonstrated the convergence of the numerical technique. Numerical results for the transient extrudate swell and jet buckling were presented and included an investigation of the effects of the parameters ε and ξ on these flows. It was found

that these parameters have a strong effect on these flows. The extrudate swell was studied for Weissenberg numbers in the range [0, 1] but depending on the parameters ε and ξ, converged solutions can be obtained at higher *We*. In contrast, for the jet buckling flow, an upper limit in the Weissenberg number was not observed. The numerical technique presented in this paper proved capable of simulating fully three-dimensional unsteady free surface flows governed by the PTT constitutive equation. However, it has some limitations that have to be addressed in the future. It is the case of the momentum equations which are solved explicitly, therefore imposing a restriction on the time-step size and consequently, realistic simulations can take many hours of CPU time. The simulations presented in this paper were performed on a computer with 16GB memory, processor Intel Xeon E5345 of 2.33 GHz. One single simulation of the extrudate swell took about 70 h while one simulation of jet buckling took an average of 50 h. Therefore, an implicit method for solving the momentum equations and the parallelization of the code would result in large gains, a code improvement to be undertaken in the future.

Acknowledgments

We gratefully acknowledge the support from the Brazilian funding agencies: FAPESP - Fundação de Amparo a pesquisa do Estado de São Paulo (project No. 04/16064–9), CNPq - Conselho Nacional de Desenvolvimento Científico e Tecnológico (grants Nos. 304422/2007-0, 470764/2007-4) and CAPES/GRICES grant No. 136/5. FTP and MAA acknowledge the funding by GRICES/CAPES project number 4.1.3(CAPES/CPLP) and by FCT through projects PTDC/EQU-FTT/71800/2006 and PTDC/EQU-FTT/70727/2006.

Appendix A.

A.1. Calculation of the non-Newtonian tensor on rigid boundaries

To obtain expressions for the components of the non-Newtonian stress tensor on rigid boundaries we extend the accurate methodology employed in the two-dimensional case (see Paulo et al. [21]) to the three-dimensional case. The components of the non-Newtonian tensor on rigid boundaries are calculated from Eq. (10) (presented in Section 4) which we assume to hold with the initial condition $S_{ij} = 0$. From Eq. (10) we obtain

$$\begin{aligned}\frac{\partial \tilde{S}_{ij}}{\partial t} &= -\epsilon\, Re\, e^{-\frac{t}{We}} \tilde{S}_{kk}\tilde{S}_{ij} - \frac{\partial(u_k \tilde{S}_{ij})}{\partial x_k} + \tilde{S}_{jk}\left(\frac{\partial u_i}{\partial x_k} - \xi D_{ik}\right) \\ &+\tilde{S}_{ik}\left(\frac{\partial u_j}{\partial x_k} - \xi D_{jk}\right) - 2\epsilon \tilde{S}_{kk} D_{ij} - \frac{2}{Re} e^{\frac{t}{We}} \left\{ \frac{\partial D_{ij}}{\partial t} + \frac{\partial(u_k D_{ij})}{\partial x_k} \right. \\ &\left. -D_{jk}\left(\frac{\partial u_i}{\partial x_k} - \xi D_{ik}\right) - D_{ik}\left(\frac{\partial u_j}{\partial x_k} - \xi D_{jk}\right) \right\}\end{aligned} \tag{A.1}$$

Eq. (A.1) is solved on rigid boundaries parallel to the *xy*-plane; rigid boundaries parallel to the *xz*-plane and rigid boundaries parallel to the *yz*-plane as follows.

A plane normal to coordinate *n* has two tangential directions u_{t_1} and u_{t_2}. From the no-slip condition we have

$$\frac{\partial}{\partial x_{t_1}} = \frac{\partial}{\partial x_{t_2}} = 0 \Rightarrow \frac{\partial u_n}{\partial x_n} = 0$$

(from continuity and no summation on n). (A.2)

Thus, only the derivatives $\partial u_i/\partial x_j$ with $i = t_1, t_2$ and $j = n$ are not zero.

Expansion of Eq. (A.1) and application of these conditions leads to a set of simplified equations. This set represents a (6×6)-nonlinear system for the unknowns $\tilde{S}_{ij}$. This nonlinear system must be calculated on all rigid boundaries for each computational cell. However, the term $Re\, e^{-(t/We)}$, which multiplies the nonlinear terms is usually considerably less than unity in which case the corresponding nonlinear terms of Eq. (A.1) may be neglected. Hence, at the cells lying at rigid boundaries Eq. (A.3) is solved after simplification with the above no-slip condition

$$\begin{aligned}\frac{\partial \tilde{S}_{ij}}{\partial t} &= +\tilde{S}_{jk}\left(\frac{\partial u_i}{\partial x_k} - \xi D_{ik}\right) + \tilde{S}_{ik}\left(\frac{\partial u_j}{\partial x_k} - \xi D_{jk}\right) - 2\epsilon \tilde{S}_{kk} D_{ij} \\ &-\frac{2}{Re} e^{\frac{t}{We}} \left\{ \frac{\partial D_{ij}}{\partial t} - D_{jk}\left(\frac{\partial u_i}{\partial x_k} - \xi D_{ik}\right) - D_{ik}\left(\frac{\partial u_j}{\partial x_k} - \xi D_{jk}\right) \right\}\end{aligned} \tag{A.3}$$

By making $t_1 = x$, $t_2 = y$ and $n = z$, the simplified form of Eq. (A.3) can be solved for $\tilde{S}_{ij}$ by integrating it over the interval $[t, t + \delta t]$.

In general form, the integrals, such as

$$\int_t^{t+\delta t} \left(\frac{\partial V}{\partial z}\tilde{S}^{lm}\right)(x, y, z, s)\, ds,$$

are approximated by the trapezoidal rule, namely

$$\begin{aligned}&\int_t^{t+\delta t} \left(\frac{\partial V}{\partial z}\tilde{S}^{lm}\right)(x, y, z, s) ds \\ &= \frac{\delta t}{2}\left[\left(\frac{\partial V}{\partial z}\tilde{S}^{lm}\right)(x, y, z, t) + \left(\frac{\partial V}{\partial z}\tilde{S}^{lm}\right)(x, y, z, t + \delta t)\right],\end{aligned}$$

where V denotes either u or v while l and m denotes either x, y or z.

Integrals like $\int_t^{t+\delta t} e^{(1/We)s}(\partial V(x, y, z, s)/\partial z) ds$ are solved by the mean value theorem, namely

$$\int_t^{t+\delta t} e^{\frac{1}{We}s} \frac{\partial V(x, y, z, s)}{\partial z} ds = e^{\frac{1}{We}t}(e^{\frac{1}{We}\delta t} - 1) We \frac{\partial V(x, y, z, t^*)}{\partial z},$$

where $t^* \in [t, t + \delta t]$, while integrals such as $\int_t^{t+\delta t} e^{(1/We)s}\partial/\partial s \left(\partial V(x, y, z, s)/\partial z\right) ds$ are calculated using integration by parts,

$$\begin{aligned}&\int_t^{t+\delta t} e^{\frac{1}{We}s} \frac{\partial}{\partial s}\left(\frac{\partial V(x, y, z, s)}{\partial z}\right) ds \\ &= e^{\frac{1}{We}t}\left[e^{\frac{1}{We}\delta t}\frac{\partial V(x, y, z, t + \delta t)}{\partial z} - \frac{\partial V(x, y, z, t)}{\partial z}\right. \\ &\left. -(e^{\frac{1}{We}\delta t} - 1)\frac{\partial V(x, y, z, t^*)}{\partial z}\right],\end{aligned}$$

where

$$\frac{\partial V(x, y, z, t^*)}{\partial z} = \frac{1}{2}\left[\frac{\partial V(x, y, z, t)}{\partial z} + \frac{\partial V(x, y, z, t + \delta t)}{\partial z}\right].$$

Thus, integrating the simplified form of Eq. (A.3) over the interval $[t, t + \delta t]$ we get,

$$\begin{aligned}\tilde{S}_{ij}^{(n+1)} &= \tilde{S}_{ij} + \frac{\delta t}{2}\left[\tilde{S}_{jk}\left(\frac{\partial u_i}{\partial x_k} - \xi D_{ik}\right) + \tilde{S}_{ik}\left(\frac{\partial u_j}{\partial x_k} - \xi D_{jk}\right)\right. \\ &\left. +\tilde{S}_{jk}^{(n+1)}\left(\frac{\partial u_i^{(n+1)}}{\partial x_k} - \xi D_{ik}^{(n+1)}\right) + \tilde{S}_{ik}^{(n+1)}\left(\frac{\partial u_j^{(n+1)}}{\partial x_k} - \xi D_{jk}^{(n+1)}\right)\right] \\ &-\delta t\, \epsilon(\tilde{S}_{jk}D_{ij} + \tilde{S}_{jk}^{(n+1)}D_{ij}^{(n+1)}) \\ &-2\frac{We}{Re} e^{\frac{t}{We}}(e^{\delta t} - 1)\left\{-D_{jk}\left(\frac{\partial u_i(t^*)}{\partial x_k} - \xi D_{ik}(t^*)\right)\right. \\ &\left. -D_{ik}\left(\frac{\partial u_j(t^*)}{\partial x_k} - \xi D_{jk}(t^*)\right)\right\} \\ &-\frac{2}{Re} e^{\frac{t}{We}}[e^{\frac{\delta t}{We}} D_{ij}^{(n+1)} - D_{ij} - (e^{\frac{\delta t}{We}} - 1)D_{ij}(t^*)]\end{aligned} \tag{A.4}$$

where $t^* \in [t, t + \delta t]$.

Eq. (A.4) represents a (6×6)-linear system for the components $\tilde{S}_{ij}^{(n+1)}$. By multiplying it by the factor $e^{-(t+\delta t/We)}$ we obtain an expression for the components of $S_{ij}^{(n+1)}$ as follows:

$$\begin{aligned} S_{ij}^{(n+1)} &= e^{-\frac{\delta t}{We}} S_{ij} + \frac{\delta t}{2}\left\{ e^{-\frac{\delta t}{We}} \left[S_{jk}\left(\frac{\partial u_i}{\partial x_k} - \xi D_{ik}\right) + S_{ik}\left(\frac{\partial u_j}{\partial x_k} - \xi D_{jk}\right)\right]\right. \\ &\left. + S_{jk}^{(n+1)}\left(\frac{\partial u_i^{(n+1)}}{\partial x_k} - \xi D_{ik}^{(n+1)}\right) + S_{ik}^{(n+1)}\left(\frac{\partial u_j^{(n+1)}}{\partial x_k} - \xi D_{jk}^{(n+1)}\right)\right\} \\ &- \delta t\,\epsilon\,[e^{-\frac{\delta t}{We}} S_{kk} D_{ij} + S_{kk}^{(n+1)} D_{ij}^{(n+1)}] \\ &- 2\frac{We}{Re}(1 - e^{-\frac{\delta t}{We}})\left\{ -D_{jk}(t^*)\left(\frac{\partial u_i(t^*)}{\partial x_k} - \xi D_{ik}(t^*)\right)\right. \\ &\left. - D_{ik}(t^*)\left(\frac{\partial u_j(t^*)}{\partial x_k} - \xi D_{jk}(t^*)\right)\right\} \\ &- \frac{2}{Re}[D_{ij}^{(n+1)} - e^{-\frac{\delta t}{We}} D_{ij} - (1 - e^{-\frac{\delta t}{We}}) D_{ij}(t^*)]. \end{aligned} \tag{A.5}$$

To solve this system of equations we expand (A.5) and substitute the equations of S_{xx}, S_{yy}, S_{zz} and S_{xy} into the equations for S_{xz} and S_{yz}. In this case we obtain the following (2×2)-linear system for the unknowns ${S_{xz}}^{(n+1)}$ and ${S_{yz}}^{(n+1)}$

$$\begin{cases} a_1 X + b_1 Y = c_1 \\ a_2 X + b_2 Y = c_2 \end{cases} \tag{A.6}$$

where $X = {S_{xz}}^{(n+1)}$ and $Y = {S_{yz}}^{(n+1)}$. The coefficients a_1, b_1 and c_1 are given by

$$\begin{aligned} a_1 &= 1 + \left[\xi(2-\xi) + 2\varepsilon(1-\xi)\right]\left(\frac{\delta t}{2}\right)^2\left(\frac{\partial u^{(n+1)}}{\partial z}\right)^2 \\ &\quad + (2-\xi)\frac{\xi}{4}\left(\frac{\delta t}{2}\right)^2\left(\frac{\partial v^{(n+1)}}{\partial z}\right)^2 \end{aligned}$$

$$b_1 = \left[\frac{3\xi}{4}(2-\xi) + \varepsilon(2-\xi) - \varepsilon\xi\right]\left(\frac{\delta t}{2}\right)^2 \frac{\partial u^{(n+1)}}{\partial z}\frac{\partial v^{(n+1)}}{\partial z}$$

$$\begin{aligned} c_1 &= e^{-\frac{1}{We}\delta t}\left\{ S_{xz} - \mathcal{C}\frac{\delta t}{2}\frac{\partial u^{(n+1)}}{\partial z}\left[S_{xx} + (2-\xi)\left(\frac{\delta t}{2}\frac{\partial u}{\partial z}S_{xz}\right.\right.\right. \\ &\left.\left.\left. + \frac{We}{Re}(e^{\frac{1}{We}\delta t} - 1)\left(\frac{\partial u(t^*)}{\partial z}\right)^2\right)\right] + (1-\mathcal{C})\frac{\delta t}{2}\frac{\partial u^{(n+1)}}{\partial z}\left[S_{zz}\right. \\ &\left. - \xi\left(\frac{\delta t}{2}\frac{\partial u}{\partial z}S_{xz} + \frac{\delta t}{2}\frac{\partial v}{\partial z}S_{yz} + \frac{We}{Re}(e^{\frac{1}{We}\delta t} - 1)\left(\left(\frac{\partial u(t^*)}{\partial z}\right)^2\right.\right.\right. \\ &\left.\left.\left. - \frac{\xi}{2}\frac{\delta t}{2}\frac{\partial v^{(n+1)}}{\partial z}\left[S_{xy} + \left(\frac{\partial v(t^*)}{\partial z}\right)^2\right)\right)\right] + (2-\xi)\left(\frac{\delta t}{4}\frac{\partial u}{\partial z}S_{yz}\right. \\ &\left. + \frac{\delta t}{4}\frac{\partial v}{\partial z}S_{xz} + \frac{We}{Re}(e^{\frac{1}{We}\delta t} - 1)\frac{\partial u(t^*)}{\partial z}\frac{\partial v(t^*)}{\partial z}\right)\Bigg] - \varepsilon\frac{\delta t}{2}\frac{\partial u^{(n+1)}}{\partial z}\left[S_{yy}\right. \\ &\left. + (2-\xi)\left(\frac{\delta t}{2}\frac{\partial v}{\partial z}S_{yz} + \frac{We}{Re}(e^{\frac{1}{We}\delta t} - 1)\left(\frac{\partial v(t^*)}{\partial z}\right)^2\right)\right] \\ &- \frac{\xi}{2}\frac{\delta t}{2}\frac{\partial u}{\partial z}S_{xx} - \frac{\xi}{2}\frac{\delta t}{2}\frac{\partial v}{\partial z}S_{xz} + (2-\xi)\frac{\delta t}{4}\frac{\partial u}{\partial z}S_{zz} \\ &- \varepsilon\frac{\delta t}{2}\frac{\partial u}{\partial z}(S_{xx} + S_{yy} + S_{zz}) \\ &\left. - \frac{1}{Re}\left[e^{\frac{\delta t}{We}}\frac{\partial u^{(n+1)}}{\partial z} - \frac{\partial u}{\partial z} - (e^{\frac{\delta t}{We}} - 1)\frac{\partial u(t^*)}{\partial z}\right]\right\} \end{aligned}$$

where $\mathcal{C} = ((\xi/2) + \varepsilon)$. The expressions for a_2, b_2, c_2 are similar to a_1, b_1, c_1. The solution of Eq. the (A.6) is given by

$${S_{xz}}^{(n+1)} = \left(\frac{c_1}{a_1} - \frac{b_1}{a_1}\frac{(a_2c_1 - a_1c_2)}{(a_2b_1 - a_1b_2)}\right) \tag{A.7}$$

$${S_{yz}}^{(n+1)} = \left(\frac{(a_2c_1 - a_1c_2)}{(a_2b_1 - a_1b_2)}\right) \tag{A.8}$$

since of course $a_1 \neq 0$ and $(a_2b_1 - a_1b_2) \neq 0$.

Once ${S_{yz}}^{(n+1)}$ and ${S_{xz}}^{(n+1)}$ have been computed, the other components of the non-Newtonian tensor S_{ij} can be calculated from Eq. (A.5).

Appendix B.

In this section we present the equations for calculating the non-Newtonian tensor S_{ij} on rigid boundaries which are parallel to the xy-plane. The equations for obtaining the tensor S_{ij} on rigid boundaries parallel to the xz- and yz-planes are obtained in the same manner and therefore they are not given here.

B.1. Boundary cells having only the bottom (or top) face contiguous with an interior cell face

Rigid boundaries parallel to the xy-plane are identified by boundary cells with the top (or bottom) face in contact with an interior cell face (F or S cell). The values of S_{xx}, S_{yy}, S_{zz}, S_{xy}, S_{xz} and S_{yz} at the centre of boundary cells are calculated from equations derived in Section A.1. For instance, if we consider Fig. B.1, then the non-Newtonian tensor S_{ij} at cell centres is obtained as follows. First, we discretize Eqs. (A.7), (A.8) and (A.5) to calculate an approximation for S_{ij} on the top face $(i, j, k + \frac{1}{2})$ of a cell as follows.

$$\begin{aligned} {S^{xx}}_{i,j,k+\frac{1}{2}}^{(n+1)} &= e^{-\frac{1}{We}\delta t}{S^{xx}}_{i,j,k+\frac{1}{2}} + (2-\xi)\frac{\delta t}{2}\left[e^{-\frac{1}{We}\delta t}\left(\frac{\partial u}{\partial z}S_{xz}\right)\Big|_{i,j,k+\frac{1}{2}}\right. \\ &\left. + \left(\frac{\partial u^{(n+1)}}{\partial z}{S_{xz}}^{(n+1)}\right)\Big|_{i,j,k+\frac{1}{2}}\right] + (2-\xi)\frac{We}{Re}(1 - e^{\frac{1}{We}\delta t})\left[\frac{\partial u(t^*)}{\partial z}\Big|_{i,j,k+\frac{1}{2}}\right]^2, \end{aligned} \tag{B.1}$$

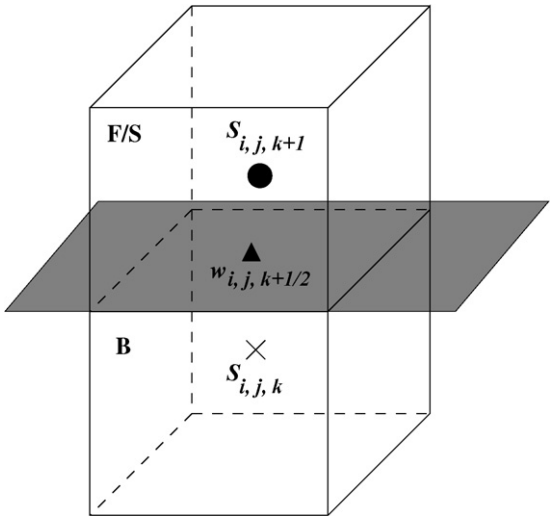

Fig. B.1. Boundary cell with the top face contiguous with an interior cell face.

$$S^{yy(n+1)}_{i,j,k+\frac{1}{2}} = e^{-\frac{1}{We}\delta t} S^{yy}_{i,j,k+\frac{1}{2}} + (2-\xi)\frac{\delta t}{2}\left[e^{-\frac{1}{We}\delta t}\left(\frac{\partial v}{\partial z} S_{yz}\right)\Big|_{i,j,k+\frac{1}{2}} + \left(\frac{\partial v^{(n+1)}}{\partial z} S_{yz}{}^{(n+1)}\right)\Big|_{i,j,k+\frac{1}{2}}\right] + (2-\xi)\frac{We}{Re}(1-e^{\frac{1}{We}\delta t})\left(\frac{\partial v(t^*)}{\partial z}\Big|_{i,j,k+\frac{1}{2}}\right)^2, \tag{B.2}$$

$$S^{zz(n+1)}_{i,j,k+\frac{1}{2}} = e^{-\frac{1}{We}\delta t} S^{zz}_{i,j,k+\frac{1}{2}} - \xi\frac{\delta t}{2}\left[e^{-\frac{1}{We}\delta t}\left(\frac{\partial u}{\partial z} S_{xz}\right)\Big|_{i,j,k+\frac{1}{2}} + \left(\frac{\partial u^{(n+1)}}{\partial z} S_{xz}{}^{(n+1)}\right)\Big|_{i,j,k+\frac{1}{2}}\right] - \xi\frac{\delta t}{2}\left[e^{-\frac{1}{We}\delta t}\left(\frac{\partial v}{\partial z} S_{yz}\right)\Big|_{i,j,k+\frac{1}{2}} + \left(\frac{\partial v^{(n+1)}}{\partial z} S_{yz}{}^{(n+1)}\right)\Big|_{i,j,k+\frac{1}{2}}\right] - \xi\frac{We}{Re}(1-e^{\frac{1}{We}\delta t})\left[\left(\frac{\partial u(t^*)}{\partial z}\Big|_{i,j,k+\frac{1}{2}}\right)^2 + \left(\frac{\partial v(t^*)}{\partial z}\Big|_{i,j,k+\frac{1}{2}}\right)^2\right], \tag{B.3}$$

$$S^{xy(n+1)}_{i,j,k+\frac{1}{2}} = e^{-\frac{1}{We}\delta t} S^{xy}_{i,j,k+\frac{1}{2}} + \left(1-\frac{\xi}{2}\right)\frac{\delta t}{2}\left[e^{-\frac{1}{We}\delta t}\left(\frac{\partial u}{\partial z} S_{yz}\right)_{i,j,k+\frac{1}{2}} + \left(\frac{\partial u^{(n+1)}}{\partial z} S_{yz}{}^{(n+1)}\right)_{i,j,k+\frac{1}{2}}\right] + \left(1-\frac{\xi}{2}\right)\frac{\delta t}{2}\left[e^{-\frac{1}{We}\delta t}\left(\frac{\partial v}{\partial z} S_{xz}\right)_{i,j,k+\frac{1}{2}} + \left(\frac{\partial v^{(n+1)}}{\partial z} S_{xz}{}^{(n+1)}\right)_{i,j,k+\frac{1}{2}}\right] + (2-\xi)\frac{We}{Re}(1-e^{\frac{1}{We}\delta t})\frac{\partial u(t^*)}{\partial z}\Big|_{i,j,k+\frac{1}{2}}\frac{\partial v(t^*)}{\partial z}\Big|_{i,j,k+\frac{1}{2}}, \tag{B.4}$$

$$S^{xz(n+1)}_{i,j,k+\frac{1}{2}} = \left(\frac{c_1}{a_1} - \frac{b_1}{a_1}\frac{(a_2c_1 - a_1c_2)}{(a_2b_1 - a_1b_2)}\right)\Big|_{i,j,k+\frac{1}{2}} \tag{B.5}$$

$$S^{yz(n+1)}_{i,j,k+\frac{1}{2}} = \left(\frac{(a_2c_1 - a_1c_2)}{(a_2b_1 - a_1b_2)}\right)\Big|_{i,j,k+\frac{1}{2}} \tag{B.6}$$

since of course $a_1|_{i,j,k+(1/2)} \neq 0$ and $(a_2b_1 - a_1b_2)|_{i,j,k+(1/2)} \neq 0$. The constants a_1, b_1, c_1, a_2, b_2 and c_2 have been defined in Section A.1.

The values of $(\partial u(t^*)/\partial z)|_{i,j,k+(1/2)}$ and $(\partial v(t^*)/\partial z)|_{i,j,k+(1/2)}$ are obtained by averaging between times t_n and t_{n+1}, namely

$$\frac{\partial u(t^*)}{\partial z}\Big|_{i,j,k+\frac{1}{2}} = \frac{1}{2}\left[\frac{\partial u}{\partial z}\Big|_{i,j,k+\frac{1}{2}} + \frac{\partial u^{(n+1)}}{\partial z}\Big|_{i,j,k+\frac{1}{2}}\right],$$

$$\frac{\partial v(t^*)}{\partial z}\Big|_{i,j,k+\frac{1}{2}} = \frac{1}{2}\left[\frac{\partial v}{\partial z}\Big|_{i,j,k+\frac{1}{2}} + \frac{\partial v^{(n+1)}}{\partial z}\Big|_{i,j,k+\frac{1}{2}}\right],$$

and the spatial derivatives are approximated by

$$\frac{\partial u}{\partial z}\Big|_{i,j,k+\frac{1}{2}} = \frac{u^n_{i,j,k+1} - u^n_{i,j,k+\frac{1}{2}}}{\delta z/2}, \quad \frac{\partial u^{(n+1)}}{\partial y}\Big|_{i,j,k+\frac{1}{2}} = \frac{u^{(n+1)}_{i,j,k+1} - u^{(n+1)}_{i,j,k+\frac{1}{2}}}{\delta z/2},$$

$$\frac{\partial v}{\partial z}\Big|_{i,j,k+\frac{1}{2}} = \frac{v^n_{i,j,k+1} - v^n_{i,j,k+\frac{1}{2}}}{\frac{\delta z}{2}}, \quad \frac{\partial v^{(n+1)}}{\partial z}\Big|_{i,j,k+\frac{1}{2}} = \frac{v^{(n+1)}_{i,j,k+1} - v^{(n+1)}_{i,j,k+\frac{1}{2}}}{\frac{\delta z}{2}}.$$

The velocities at $(i, j, k+1)$ are given by

$$u_{i,j,k+1} = \frac{u_{i+\frac{1}{2},j,k+1} + u_{i-\frac{1}{2},j,k+1}}{2} \quad \text{and} \quad v_{i,j,k+1} = \frac{v_{i,j+\frac{1}{2},k+1} + v_{i,j-\frac{1}{2},k+1}}{2},$$

respectively. Finally, the values of $S^{xx}_{i,j,k}$, $S^{yy}_{i,j,k}$, $S^{zz}_{i,j,k}$, $S^{xy}_{i,j,k}$, $S^{xz}_{i,j,k}$ and $S^{yz}_{i,j,k}$ are obtained using linear interpolation between the nodes $(i, j, k+(1/2))$ and $(i, j, k+1)$.

References

[1] M.A. Alves, F.T. Pinho, P.J. Oliveira, Study of steady pipe and channel flows of a single-mode Phan-Thien–Tanner fluid, J. Non-Newtonian Fluid Mech. 101 (2001) 55–76.
[2] M.A. Alves, P.J. Oliveira, F.T. Pinho, A convergent and universally bounded interpolation scheme for the treatment of advection, Int. J. Numer. Meth. Fluids 41 (2003) 47–75.
[3] M.A. Alves, P.J. Oliveira, F.T. Pinho, Benchmark solutions for the flow of Oldroyd-b and PTT fluids in planar contractions, J. Non-Newtonian Fluid Mech. 110 (2003) 45–75.
[4] M.A. Alves, F.T. Pinho, P.J. Oliveira, Viscoelastic flow in a 3D Square/square contraction, J. Rheol. 52 (2003) 1347–1368.
[5] G.K. Batchelor, An Introduction of Fluid Dynamics, Cambridge University Press, Cambridge, 1967.
[6] A. Bonito, M. Picasso, M. Laso, Numerical simulation of 3d viscoelastic flows with free surfaces, J. Comput. Phys. 215 (2006) 691–716.
[7] D. Bousfield, R. Keunings, M. Denn, Transient deformation of an inviscid inclusion in a viscoelastic extensional flow, J. Non-Newtonian Fluid Mech. 27 (1988) 205–221.
[8] D. Bousfield, R. Keunings, G. Marruci, M. Denn, Nonlinear analysis of the surface tension driven breakup of viscoelastic filaments, J. Non-Newtonian Fluid Mech. 21 (1986) 79–97.
[9] A. Castelo, M.F. Tomé, C.N.L. César, S. McKee, J.A. Cuminato, Freeflow: an integrated simulation system for three-dimensional free surface flows, J. Comput. Visual. Sci. 2 (2000) 199–210.
[10] M.J. Crochet, R. Keunings, Finite element analysis of die-swell of a highly elastic fluid, J. Non-Newtonian Fluid Mech. 10 (1982) 339–356.
[11] J.O. Cruickshank, Low-Reynolds-number instabilities in stagnating jet flows, J. Fluid Mech. 193 (1988) 111–127.
[12] J.O. Cruickshank, B.R. Munson, Viscous-fluid buckling of plane axisymmetric jets, J. Fluid Mech. 113 (1981) 221–239.
[13] F.H. Harlow, J.E. Welch, The MAC method, Phys. Fluids 8 (1965) 2182–2189.
[14] R. Keunings, An algorithm for the simulation of transient viscoelastic flows with free surfaces, J. Comput. Phys. 62 (1986) 199–220.
[15] R. Keunings, D. Bousfield, Analysis of surface tension driven leveling in horizontal viscoelastic films, J. Non-Newtonian Fluid Mech. 22 (1987) 219–233.
[16] J.M. Marchal, M.J. Crochet, A new mixed finite element for calculating viscoelastic flow, J. Non-Newtonian Fluid Mech. 26 (1987) 77–114.
[17] G. Mompean, M. Deville, Unsteady finite volume of Oldroyd-B fluid through a three-dimensional planar contraction, J. Non-Newtonian Fluid Mech. 72 (1997) 253–279.
[18] P.J. Oliveira, F.T. Pinho, Analytical solution for fully developed channel and pipe flow of Phan-Thien–Tanner fluids, J. Fluid Mech. 387 (1999) 271–280.
[19] G.S. Paulo, Solução numérica do modelo PTT para escoamentos incompressíveis com superfícies livres, Ph.D. thesis, ICMC/USP, 2006 (in Portuguese).
[20] G.S. Paulo, M.F. Tomé J.A. Cuminato, A. Castelo, Exact solution of the SPTT model for fully developed channel flows, Proceedings of COBEM 2005 (Ouro Preto - MG), CD-ROM, 2005.
[21] G.S. Paulo, M.F. Tomé, S. McKee, A marker-and-cell approach to viscoelastic free surface flows using the PTT model, J. Non-Newtonian Fluid Mech. 147 (2007) 149–174.
[22] N. Phan-Thien, R.I. Tanner, A new constitutive equation derived from network theory, J. Non-Newtonian Fluid Mech. 2 (1977) 353–365.
[23] D. Rajagopalan, R.C. Armstrong, R.A. Brown, Finite element methods for calculation of steady viscoelastic flow using constitutive equations with a Newtonian viscosity, J. Non-Newtonian Fluid Mech. 36 (1990) 159–192.
[24] N.M. Ribe, A general theory of the dynamics of thin viscous sheets, J. Fluid Mech. 457 (2002) 255–283.
[25] N.M. Ribe, Periodic folding of viscous jets, Phys. Rev. E 68 (2003), Art. No. 036305 Part 2.
[26] N.M. Ribe, Coiling of viscous jets, Proc. R. Soc. Lond. Series A - Math. Phys. Eng. Sci. 460 (2004) 3223–3239.
[27] M.E. Ryan, A. Dutta, A finite difference simulation of extrudate swell, in: Proceedings of Second World Congress of Chemical Engineering, 1981, pp. 277–281.
[28] R.I. Tanner, A theory of die-swell, J. Pol. Sci. 8 (1970) 2067–2078.
[29] M.F. Tomé, L. Grossi, A. Castelo, J.A. Cuminato, N. Mangiavacchi, V.G. Ferreira, F.S. Sousa, S. McKee, A numerical method for solving three-dimensional generalized Newtonian free surface flows, J. Non-Newtonian Fluid Mech. 123 (2004) 85–103.
[30] M.F. Tomé, A. Castelo, J.A. Cuminato, N. Mangiavacchi, S. McKee, GENSMAC3D: a numerical method for solving unsteady three-dimensional free surface flows, Int. J. Numer. Meth. Fluids 37 (2001) 747–796.
[31] M.F. Tomé, A. Castelo, V.G. Ferreira, S. McKee, A finite difference technique for solving the Oldroyd-B model for 3D-unsteady free surface flows, J. Non-Newtonian Fluid Mech. 154 (2008) 179–206.
[32] M.F. Tomé, B. Duffy, S. McKee, A numerical technique for solving unsteady non-Newtonian free surface flows, J. Non-Newtonian Fluid Mech. 62 (1996) 9–34.

[33] M.F. Tomé, N. Mangiavacchi, A. Castelo, J.A. Cuminato, S. McKee, A finite difference technique for simulating unsteady viscoelastic free surface flows, J. Non-Newtonian Fluid Mech. 106 (2002) 61–106.
[34] M.F. Tomé, S. McKee, GENSMAC: a computational marker-and-cell method for free surface flows in general domains, J. Comput. Phys. 110 (1994) 171–186.
[35] S. Xue, N. Phan-Thien, R.I. Tanner, Numerical study of secondary flows of viscoelastic fluid in straight pipes by an implicit finite volume method, J. Non-Newtonian Fluid Mech. 59 (1995) 191–213.
[36] S. Xue, N. Phan-Thien, R.I. Tanner, Numerical study of secondary flows of viscoelastic fluid in straight pipes by an implicit finite volume method, J. Non-Newtonian Fluid Mech. 74 (1998) 195–245.